

# Coupled-channel approach to isotensor $\pi\pi\pi$ scattering from lattice QCD

Yuchuan Feng,<sup>1,\*</sup> Chris Culver,<sup>2,†</sup> Michael Döring,<sup>1,3,‡</sup>  
Maxim Mai,<sup>4,1,§</sup> Andrei Alexandru,<sup>1,5,¶</sup> and Frank X. Lee<sup>1, \*\*</sup>

<sup>1</sup>*The George Washington University, Washington, DC 20052, USA*

<sup>2</sup>*Groq Inc, 3 Hammersmith Grove, London, UK*

<sup>3</sup>*Thomas Jefferson National Accelerator Facility, Newport News, VA 23606, USA*

<sup>4</sup>*Albert Einstein Center for Fundamental Physics, Institute for Theoretical Physics,  
University of Bern, Sidlerstrasse 5, 3012 Bern, Switzerland*

<sup>5</sup>*Department of Physics, University of Maryland, College Park, MD 20742, USA*

The quest to understand three-body dynamics from first-principle QCD includes the study of non-resonant and resonant systems. The isospin  $I = 2$  system is of particular interest having no three-body resonance but featuring a resonance in a sub-channel, while also being a coupled-channel problem. In this study, we calculate the finite-volume spectrum from lattice QC at two different pion masses, map the amplitude to the infinite volume through a generalized FVU three-body quantization condition, investigate the limit of a narrow  $\rho$ , and compare with an effective Lagrangian prediction at leading order. Chiral extrapolations between different pion masses are performed.

## CONTENTS

I. Introduction	2
II. Formalism	3
A. Coupled-channel three-body scattering amplitude	3
B. Coupled-channel three-body quantization condition	6
III. Lattice QCD spectrum	10
A. Lattice QCD setup	10
B. Fits to lattice finite-volume spectrum	12
IV. Coupled-channel Dynamics	15
A. Dynamics at the $\pi\rho$ threshold	15
B. Singular behavior of the contact term	16
C. Comparison with an effective Lagrangian	17
V. Infinite-volume amplitude	19
A. Three-body amplitude	19
B. Narrow $\rho$ -limit	22
VI. Conclusions	24
Acknowledgments	24
References	25

\* [fengyuchuan@gwmail.gwu.edu](mailto:fengyuchuan@gwmail.gwu.edu)

† [chris.a.culver@gmail.com](mailto:chris.a.culver@gmail.com)

‡ [doring@gwu.edu](mailto:doring@gwu.edu)

§ [maxim.mai@faculty.unibe.ch](mailto:maxim.mai@faculty.unibe.ch)

¶ [aalexan@gwu.edu](mailto:aalexan@gwu.edu)

\*\* [fxlee@gwu.edu](mailto:fxlee@gwu.edu)

## I. INTRODUCTION

Quantum Chromodynamics (QCD) dictates the dynamics of strongly interacting matter. Its quantum states, the hadrons, exhibit a complex mass and decay pattern that is difficult to explain directly from QCD. Many theoretical tools have been developed in the past to address this issue. Among others, the recently most applied methods are Effective Field Theories (EFTs), lattice QCD (LQCD), and functional methods; for a recent review see Ref. [1]. One complication in resolving the resonant hadron spectrum is that the window in which their multi-hadron decay products (three or more) can be safely ignored is usually small. Already the first excited state of the nucleon, the so-called Roper-resonance  $N^*(1440)1/2^+$ , is above the  $\pi\pi N$  threshold, decaying substantially into effective three-body channels  $\pi f_0(500)$  and  $\pi\Delta$  leading to the unusual line shape of that resonance [2–4].

In recent years, approaching three-body systems from LQCD has become possible due to two closely intertwined factors. First, the increased computational capacities and algorithmic developments made the implementation of multi-hadron operators possible, see Refs. [5–21]. Typically, such programs provide a discrete finite-volume energy spectrum, which encodes the full QCD dynamics. Relating this spectrum to the infinite-volume (coupled-channel) amplitude is accomplished by the so-called Quantization Conditions (QC). Development and application of QCs is the second step, see Refs. [20–80], papers comparing different approaches [52, 81, 82], and Refs. [83, 84] for dedicated reviews and Ref. [85] for a recent status overview. A third analysis step requires the analytic continuation of the amplitude to the resonance poles to determine resonance poles position and residues, corresponding to masses and branching ratios. For three-body states, this is a nontrivial step [86–89], see also a recent review [90].

Through these developments several repulsive systems of maximal isospin have been studied:  $\pi^+\pi^+\pi^+$  [9–11, 46, 91],  $K^+K^+K^+$  [12],  $\pi^+\pi^+K^+$ ,  $K^+K^+\pi^+$  [18] and a comprehensive analysis of all of them [92]. A first resonant  $\pi\pi\pi$  system from LQCD has been studied for the  $I^G = 1^-$ ,  $J^{PC} = 1^{++}$  quantum numbers of the  $a_1(1260)$  [16] in  $\pi\rho$  coupled  $S$ - and  $D$ -wave channels. In Ref. [19] the three-pion system with  $\omega(782)$  quantum numbers was analyzed, and in Ref. [21] the excited pion spectrum was studied revealing evidence of a resonance that could correspond to the  $\pi(1300)$ .

In this paper we calculate and analyze the intermediate-isospin  $I = 2$  three-pion system, similar to a recent analysis [93]. This system is simpler than the  $I = 1$  system as there is no three-body resonance and there are fewer channels referring to different possibilities to arrange the total isospin. It is still different from systems at maximal isospin because there is a resonance in a sub-channel (“*isobar*”), the  $\rho(770)$ . After calculating the finite-volume spectrum of this system at two different pion masses, the three-body QC is extended to the appropriate coupled channel system, including all isobars up to  $P$ -wave. This is necessary since  $I = 2$  can be built either by combining a  $\rho$ -meson with a pion or, alternatively, by combining the isotensor  $\pi\pi$ -system in  $S$ -wave, referred to as to “*isograviton*”,  $G$ , with another pion. Comprehensive studies of (iso)spin structures and channels with pions and kaons, for (non)strange systems were recently conducted in Refs. [94] and [95] for up to nine channels.

After the derivation of the QC, we study technical aspects, such as the cutoff dependence. We find that by over-subtracting the one-particle exchange term the volume dependence of the cutoff can be reduced. This approach is then used to study the finite-volume spectrum calculated on the lattice. In particular, the unknown three-body force for different coupled-channels is fitted for several channel combinations and cutoffs. Then, the infinite volume amplitude is calculated including the quantification of uncertainties.

Besides LQCD, effective field theories provide another systematic approach to strong interactions, see, e.g., Refs. [1, 96–99] for related reviews. In the present work, we study the predictive power of a particular effective Lagrangian of  $\pi\rho$  interactions [100] that has been used to study the nature of axial resonances hadronic molecules [101, 102]. Effective Lagrangians also provide an ordering in energy and momenta that guides the construction and constrains the form of phenomenological contact terms in fits to lattice data.

Besides low energies, another limit to be explored is the one of a narrow  $\rho$ . In that case, the three-body equation becomes a two-body equation and results can be represented in terms of phase-shifts and inelasticities. In that respect, it is of interest to compare to Ref. [103] in which the  $\rho$  is a bound state at almost twice the pion mass than in the present study, which requires a chiral extrapolation for which the above-mentioned Lagrangian of Ref. [100] is used again.

This paper is organized as follows. In Sect. II we provide the details of the formalism including the extension to coupled channels. There we also summarize the corresponding three-body quantization condition providing a comprehensive set of equations. Finally, cutoff effects are studied and modification of the scheme is provided to ensure better convergence. In Sect. IV we provide a qualitative analysis of various aspects of the coupled-channel dynamics. In that, the cutoff dependence of the contact term is studied as well as the prediction from effective field theories. In Sect. V we provide the lattice QCD finite-volume spectrum and quantitative analysis of this spectrum through the FVU three-body quantization condition. The section is finalized providing infinite-volume results. The paper is concluded in Sect. VI.

## II. FORMALISM

### A. Coupled-channel three-body scattering amplitude

The unitary three-body scattering amplitude for the process  $\pi(p_1)\pi(p_2)\pi(p_3) \rightarrow \pi(p'_1)\pi(p'_2)\pi(p'_3)$  can be re-written using cluster decomposition in terms of a two-body cluster (“isobar”) and a third particle (“spectator”) as [32, 104]

$$\langle p'_1 p'_2 p'_3 | T_3(s) | p_1 p_2 p_3 \rangle = \frac{1}{3!} \sum_{i,j} \sum_{m,n} v_j(\mathbf{p}'_{\bar{n}}, \mathbf{p}'_{\bar{n}}) \left( \tilde{\tau}_j(\sigma_{p'_n}) T_{ji}(s, \mathbf{p}'_n, \mathbf{p}_m) \tilde{\tau}_i(\sigma_{p_m}) + 2E_{p_n} (2\pi)^3 \delta^3(\mathbf{p}'_n - \mathbf{p}_m) \delta_{ji} \tilde{\tau}_i(\sigma_{p_m}) \right) v_i(\mathbf{p}_{\bar{m}}, \mathbf{p}_{\bar{m}}), \quad (2.1)$$

where  $i/j$  denote a combined index of quantum number of the in-/out-going isobar-spectator states in order. The total energy-squared is denoted by  $s = P_3^2$  for the total four-momentum  $P_3$ . The invariant mass-squared of the isobar is  $\sigma_q = s + m^2 - 2\sqrt{s}E_q$  where  $E_q = \sqrt{m^2 + q^2}$ ,  $q = |\mathbf{q}|$  and  $m = m_\pi$  is the spectator mass. In each occurrence  $\bar{x} \in \{1, 2, 3\} \setminus \{x\}$  (i.e.,  $\bar{x}$  can be anything but  $x$ ) and  $\bar{\bar{x}} \in \{1, 2, 3\} \setminus \{x, \bar{x}\}$  (i.e.,  $\bar{\bar{x}}$  can be anything but  $x$  or  $\bar{x}$ ). Note that we have unified the notation compared to that of Refs. [32, 104] to ensure the consistency within the present article. The first summand on the right-hand side of the previous equation represents the fully connected isobar-spectator ( $T_{ij}$ ) interaction with the amplitude

$$T_{ji}(s, \mathbf{p}', \mathbf{p}) = \tilde{B}_{ji}(s, \mathbf{p}', \mathbf{p}) + \tilde{C}_{ji}(s, \mathbf{p}', \mathbf{p}) + \int \frac{d^3 l}{(2\pi)^3} \left( \tilde{B}_{jk}(s, \mathbf{p}', \mathbf{l}) + \tilde{C}_{jk}(s, \mathbf{p}', \mathbf{l}) \right) \frac{\tilde{\tau}_k(\sigma_l)}{2E_l} T_{ki}(s, \mathbf{l}, \mathbf{p}). \quad (2.2)$$

Here, the sum over repeating channel indices  $k$  is implied. Note also that, in principle,  $\tilde{\tau}$  can have sub-channels [94, 95] (i.e., different decay channels of the same quantum numbers) which are absent in the present approach so here it carries only one channel index,  $k$ .

In this study we consider isospin  $I = 2$  scattering of three pions with total angular momentum  $J = 1$ , i.e.,  $I^G(J^{PC}) = 2^-(1^{+-})$  in the three-body center of mass,  $\mathbf{P}_3 = \mathbf{0}$ . This differs from the  $a_1(1260)$  channel by the isospin. For these quantum numbers, all possible pion isobars up to spin 1 are considered, i.e., the isovector  $I_I = 1$   $\rho$  channel and the isotensor  $I_I = 2$  channel abbreviated as  $G$  (“isograviton”) in the following. This defines possible isobar-spectator channels in the helicity basis as  $HB = \{\pi\rho(\lambda = -1), \pi\rho(\lambda = 0), \pi\rho(\lambda = +1), \pi G(\lambda = 0)\}$ , denoting the helicity of the vector-meson by  $\lambda$ . We describe the matching of two-body amplitudes at the end of this section and, first, discuss the channel transitions between the  $\pi\rho$  and the  $\pi G$  channels.

In the plane-wave basis, we denote the transition amplitude from channel  $i$  to  $j$  as [94]

$$\tilde{B}_{ji}(s, \mathbf{p}', \mathbf{p}) = \frac{\tilde{I}_F v_j^*(p, P_3 - p - p') v_i(p', P_3 - p - p')}{2E_{\mathbf{p}'+\mathbf{p}}(\sqrt{s} - E_{\mathbf{p}} - E_{\mathbf{p}'} - E_{\mathbf{p}'+\mathbf{p}}) + i\epsilon} \quad \text{for } i, j \in HB, \quad (2.3)$$

with the angular structures of  $P$ - and  $S$ -wave isobar decay vertices, respectively,

$$v_i(p, p') = \begin{cases} \epsilon_{\lambda(i), \mu}(\mathbf{p} + \mathbf{p}')(p - p')^\mu & \text{for } i < 4 \text{ (}\rho\text{ of helicity } \lambda\text{)} \\ 1 & \text{for } i = 4 \text{ (}\mathcal{G}\text{)} \end{cases} \quad (2.4)$$

The incoming  $\rho$ -meson, that is not in its center of mass, is parametrized through the polarization vector  $\epsilon$  [105] while the outgoing one is expressed through the complex conjugate,  $\epsilon^*$ . Explicit expressions can be found, e.g., in Ref. [16].

These vertices merely contain the angular structure of the two-body sub-amplitudes, that have their isospin structure absorbed in the definition of the  $\tilde{\tau}$  [94]. This allows one to express the isospin coefficients of the transitions as simple re-coupling of Clebsch-Gordan (CG) coefficients,

$$\tilde{I}_F = \sum_{\substack{m,n \\ m',n'}} (I_I n \ I_S m | II_3) (I_{I'} n' \ I_{S'} m' | II_3) (I_x n - m' \ I_{S'} m' | I_I n) (I_x n - m' \ I_S m | I_{I'} n') . \quad (2.5)$$

As Eq. (2.5) shows, these coefficients describe how an exchanged particle of isospin  $I_x$  couples to the isospin  $I_I$  ( $I_{I'}$ ) of incoming (outgoing) isobar and the isospin  $I_S$  ( $I_{S'}$ ) of incoming (outgoing) spectator (the particle phases associated with  $\pi^+$  and  $\rho^+$  always cancel). These isospins are then combined to total isospin  $I$  with third component  $I_3$ . For the total isospin  $I = 2$  (for any  $I_3$ ) the elements read

$$\tilde{I}_F(I = 2) : \quad \begin{array}{c|cc} \pi\rho & \pi G \\ \hline \pi\rho & 1/2 & \sqrt{3}/2 \\ \pi G & \sqrt{3}/2 & -1/2 \end{array} . \quad (2.6)$$

This clear separation of isospin structure associated with the exchange and with the propagation is different from previous work [16, 88, 106], in which Lagrangians were used to calculate isospin coefficients. We, therefore, introduce the “tilde” notation here to distinguish it from previous work. For example, the  $\pi\rho \rightarrow \pi\rho$  transition  $\tilde{B}$  is half the size of  $B$  of these previous studies, while a factor of two is absorbed in  $\tilde{\tau}$  compared to the previous  $\tau$ . The calculation of  $\tilde{I}_F$  in terms of CG allows one to use isobar amplitudes as “black boxes” in contrast to using Lagrangians that always contain isospin factors of the isobars themselves. See Ref. [94] for further discussions.

The partial-wave decomposition of the scattering equation (2.2) proceeds in the same way as in Refs. [16, 88, 106]. See Ref. [94] for the chosen convention. In particular, the partial-wave projection is obtained by

$$\tilde{B}_{ji}(s, p', p) = 2\pi \int_{-1}^1 dz d_{\lambda(j)\lambda(i)}^J(z) \tilde{B}_{ji}(s, \mathbf{p}', \mathbf{p}) , \quad (2.7)$$

where  $z = \cos\theta$  for  $\theta$  being the scattering angle between  $\mathbf{p}$  and  $\mathbf{p}'$ . Note that for the spinless  $\pi G$  channel,  $\lambda = 0$ . This expression is given in the helicity basis (*HB*), while in the *JLS* basis the  $\pi\rho$  channel can couple to  $J = 1$  in relative *S*- and *D*-wave, and  $\pi G$  couples in *P*-wave, i.e.,  $JLS = \{\pi\rho(L = 0), \pi G(L = 1), \pi\rho(L = 2)\}$ . The transformation between both bases follows from Ref. [105] as

$$\tilde{B}_{L'L}(s, p', p) = U_{L'\lambda(j)} \tilde{B}_{ji}(s, p', p) U_{\lambda(i)L} \quad \text{for } L, L' \in JLS , \quad (2.8)$$

$$U_{L\lambda} = \sqrt{\frac{2L+1}{2J+1}} \sum_{\lambda_2} (L0 \ S\lambda | J\lambda) (S_1 \lambda_1 \ S_2 - \lambda_2 | S\lambda) = \sqrt{\frac{2L+1}{2J+1}} (L0 \ S\lambda | J\lambda) , \quad (2.9)$$

where  $S_1 = S$  ( $\lambda_1 = \lambda$ ) is the spin (helicity) of the isobar and  $S_2 = 0$  ( $\lambda_2 = 0$ ) is the spin (helicity) of the spectator. Note that for  $\pi\rho$ ,

$$U = \begin{pmatrix} \frac{1}{\sqrt{3}} & \frac{1}{\sqrt{3}} & \frac{1}{\sqrt{3}} \\ \frac{1}{\sqrt{6}} & -\sqrt{\frac{2}{3}} & \frac{1}{\sqrt{6}} \end{pmatrix} , \quad (2.10)$$

where the first and second rows denote *S*- and *D*-wave, respectively. For the  $\pi G$  channel,  $U = 1$ . After projection, the infinite-volume, partial-wave projected isobar-spectator equation reads

$$T_{L'L}(s, p', p) = \tilde{B}_{L'L}(s, p', p) + \tilde{C}_{L'L}(s, p', p) + \int_0^\Lambda \frac{dq q^2}{(2\pi)^3 2E_q} \left( \tilde{B}_{L'L''}(s, p', q) + \tilde{C}_{L'L''}(s, p', q) \right) \tilde{\tau}_{L''}(\sigma_q) \tilde{T}_{L''L}(s, q, p) , \quad (2.11)$$

where  $\tilde{\tau}_0 = \tilde{\tau}_2 = \tilde{\tau}_\rho$  and  $\tilde{\tau}_1 = \tilde{\tau}_G$ . As a last step, we discuss the matching of the two-body sub-amplitudes to the isobars  $\tilde{\tau}_\rho$  and  $\tilde{\tau}_G$ . Ultimately they are parametrized through phase shifts that are obtained in an intermediate step from the Inverse Amplitude Method [107, 108] (IAM). The IAM amplitude represents the two-body amplitude obtained at the same unphysical pion masses as in the present LQCD calculations (see Sect. III), encoded in the low-energy constants (LECs) of Ref. [109].

Suppressing the channel index, the IAM partial-wave amplitudes in isospin  $I_I$  are normalized according to Ref. [110]

$$t^{I_I \ell}(p', p) = \frac{1}{32N\pi} \int_{-1}^1 dx P_\ell(x) t^{I_I}(p', p), \quad (2.12)$$

where we use small  $t$  and  $\ell$  for two-body sub-amplitudes and their angular momentum ( $\ell = S$  from Eq. (2.9)) to distinguish them from the isobar-spectator amplitude  $T$  and their relative angular momentum  $L$ . For identical particles like pions in any isospin,  $N = 2$ . The inversion is given by

$$t^{I_I}(p', p) = 64N\pi^2 \sum_{\ell, m} Y_{\ell m}^*(\hat{p}') t^{I_I \ell}(p', p) Y_{\ell m}(\hat{p}). \quad (2.13)$$

Notably, it is the plane-wave  $t^{I_I}$  that enters the amplitude (2.2). No symmetry factors  $N$  should be absorbed in its definition, which is, indeed, the case here, because that factor is only present in the partial-wave projected amplitude  $t^{I_I \ell}$ . As discussed in the context of Eq. (2.5), the isospin structure of the transitions is clearly separated from that of the isobars, meaning that for  $S$ -wave,  $I_I = 2$  we simply have

$$\tilde{\tau}_G = -t^2 = -32\pi t^{20} \quad (2.14)$$

with the minus sign originating from an opposite sign in the definition of the  $T$ -matrix in the IAM vs. the current formulation. For the  $\rho$ -channel in its center of mass, one can use that

$$\epsilon_\lambda^\mu(p)p_\mu = -|\mathbf{p}| \sqrt{\frac{4\pi}{3}} Y_{1\lambda}(\theta_p, \phi_p), \quad \lambda = -1, 0, +1 \quad (2.15)$$

for a vector meson at rest to rewrite Eq. (2.13) as

$$t^1(p', p) = \frac{96\pi}{\mathbf{p}^2} t^{11} \sum_\lambda \epsilon_\lambda^\mu p_\mu \epsilon_\lambda^{\nu*} p'_\nu = \frac{24\pi}{\mathbf{p}^2} t^{11} \sum_\lambda v_{\rho, \lambda}(p, \tilde{p}) v_{\rho, \lambda}^*(p', \tilde{p}') = 96\pi \cos \theta t^{11}, \quad (2.16)$$

with  $v$  from Eq. (2.4),  $\theta$  is the scattering angle,  $p^0 = \tilde{p}^0$ ,  $\mathbf{p} = -\tilde{\mathbf{p}}$ ,  $p'^0 = \tilde{p}'^0$ , and  $\mathbf{p}' = -\tilde{\mathbf{p}}'$ . The second to last expression allows one to identify vertices  $v$  that are re-shuffled to the  $B$ -term of Eq. (2.3). The remainder is identified with  $\tilde{\tau}$  according to:

$$\tilde{\tau}_\rho(\sigma) = -\frac{24\pi}{p^2} t^{11}(\sigma) \quad (2.17)$$

with  $p = |\mathbf{p}|$  the  $\pi\pi$  magnitude of the center of mass three-momentum defined in the rest frame of the  $\rho$ -meson.

This concludes the identification of the isobar-spectator propagation with IAM amplitudes which can also be directly expressed in terms of observables, noting that for any isospin and partial wave

$$t^{I_I \ell}(\sigma) = \frac{\sqrt{\sigma}}{2} \frac{1}{(p \cot \delta^{I_I \ell} - ip)}, \quad (2.18)$$

leading to

$$-\frac{p^2}{24\pi} \frac{2}{\sqrt{\sigma}} (p \cot \delta^{I_I \ell} - ip) = \frac{1}{\tilde{\tau}_\rho(\sigma)} = \tilde{K}_\rho^{-1}(\sigma) - \Sigma_\rho^{\text{IV}}(\sigma), \quad (2.19)$$

$$-\frac{1}{32\pi} \frac{2}{\sqrt{\sigma}} (p \cot \delta^{I_I \ell} - ip) = \frac{1}{\tilde{\tau}_G(\sigma)} = \tilde{K}_G^{-1}(\sigma) - \Sigma_G^{\text{IV}}(\sigma), \quad (2.20)$$

that can be cast in terms of a real-valued  $K$ -matrix like function  $\tilde{K}$  and a loop function  $\Sigma^{\text{IV}}$ ,

$$\begin{aligned}\tilde{K}_\rho^{-1}(\sigma) &= -\frac{p^3 \cot \delta^{11}}{12\pi\sqrt{\sigma}} + \text{Re } \Sigma_\rho^{\text{IV}}(\sigma), \quad \Sigma_\rho^{\text{IV}}(\sigma) = \frac{1}{48\pi^2} \int dk \frac{\sigma^2}{E_k^5} \frac{k^4}{\sigma - 4E_k^2}, \\ \tilde{K}_G^{-1}(\sigma) &= -\frac{p \cot \delta^{20}}{16\pi\sqrt{\sigma}} + \text{Re } \Sigma_G^{\text{IV}}(\sigma), \quad \Sigma_G^{\text{IV}}(\sigma) = \frac{1}{64\pi^2} \int dk \frac{\sigma^2}{E_k^5} \frac{k^2}{\sigma - 4E_k^2}.\end{aligned}\quad (2.21)$$

With these equations, the three-to-three scattering amplitude is fully defined. In that, the only unknowns are encoded in the two-body input  $\tilde{K}$  and three-body force  $\tilde{C}$ . Their determination from data or effective field theories will be discussed in the following sections.

### B. Coupled-channel three-body quantization condition

Having fixed the infinite-volume three-body scattering amplitude in the previous section, we are now in the position to write down the corresponding three-body coupled-channel quantization condition. Individual stepping stones of the derivation have been discussed in Refs. [32, 46, 47].

The finite-volume spectrum in  $\{E_0, E_1, \dots\}^\Gamma$  in a given irreducible representation of the  $O_h$  group  $\Gamma$  is predicted through the following condition

$$\sqrt{s} \in \{E_0, E_1, \dots\}^\Gamma \iff T_\Gamma(s) = \infty. \quad (2.22)$$

The quantity on the right represents a finite-volume equivalent of the three-body scattering amplitude obtained by discretizing all momenta in the three-body scattering amplitude  $T(\sqrt{s})$ , corresponding to a cubic box of size  $L$  with periodic boundary conditions. Specifically, the allowed momenta are  $\mathcal{S}_L = 2\pi/L \cdot \mathbb{Z}^3$  which means that in the finite-volume the Eq. (2.1) becomes a matrix equation over the  $\mathcal{S}_L \times HB$  space for the helicity/channel space  $HB = \{\pi\rho(\lambda = -1), \pi\rho(\lambda = 0), \pi\rho(\lambda = +1), \pi G(\lambda = 0)\}$ . Note that the helicity of the spinless  $\pi\pi$  isobar  $G$  is given by 0, which allows one to use the same Wigner-D formulas as for the  $\rho$ -meson. In this discretized form the equations occurring in Eq. (2.2) can be solved directly leading together with the disconnected part to the following three-body quantization condition

$$\text{Method 1: } \sqrt{s} \in \{E_0, E_1, \dots\}^\Gamma \iff \left\langle E_L \left[ (\tilde{K}^{-1}(s) - \Sigma^{FV}(s)) E_L - (\tilde{B}(s) + \tilde{C}(s)) \right]^{-1} E_L \right\rangle_\Gamma = \infty. \quad (2.23)$$

Here,  $\langle \dots \rangle_\Gamma$  denotes the projection to the irrep  $\Gamma$ . Note that this corresponds to solving the discretized scattering equation in the plane-wave basis before projection to irreps, requiring a suitable labeling of involved three-momenta  $\mathbf{p}_i$ . For completeness we provide the explicit form of the quantities in Eq. (2.23) in the following. First, the elements of the one-pion exchange matrix read

$$\left[ \tilde{B}(s) \right]_{(\mathbf{p}', j)(\mathbf{p}, i)} = \tilde{I}_{ji} \frac{v_j^*(p, P_3 - p - p') v_i(p', P_3 - p - p')}{2E_{\mathbf{p}'+\mathbf{p}}(\sqrt{s} - E_{\mathbf{p}} - E_{\mathbf{p}'} - E_{\mathbf{p}'+\mathbf{p}})}, \quad \tilde{I}_{ji} = \frac{1}{2} \begin{pmatrix} 1 & 1 & 1 & \sqrt{3} \\ 1 & 1 & 1 & \sqrt{3} \\ 1 & 1 & 1 & \sqrt{3} \\ \sqrt{3} & \sqrt{3} & \sqrt{3} & -1 \end{pmatrix}_{ji} \quad (2.24)$$

where  $\tilde{I}_{ji}$  denote the isospin factors of the  $\pi\rho/\pi G$  terms to the total Isospin  $I = 2$ . Next, the self-energy of the  $\pi\pi$  pair is defined combining the infinite- and finite-volume expressions in the energy region  $Reg = [\sqrt{s_2}, \sqrt{s_2} + 0.1(\sqrt{s_{phys}} - \sqrt{s_1})]$  for  $\sqrt{s_{1/2}} = (E_p \pm |p|)$  and  $\sqrt{s_{phys}} = \sqrt{\mathbf{p}^2 + 4m_\pi^2} + E_p$ . This is necessary since Lorentz-invariance is broken on the lattice and the two-body self-energy needs to be determined in the boosted system with respect to the three-body rest frame. Technically these boosts are defined only outside of the above energy region and, thus, matching is performed

as

$$[\Sigma^{FV}(s)]_{(\mathbf{p}',j)(\mathbf{p},i)} = \delta_{\mathbf{p}'\mathbf{p}} \left\{ \begin{array}{ll} \delta_{ji} \Sigma_j^{\text{IV}}(\sigma_p) & \text{for } \sqrt{s} \in \text{Reg} \\ \left( \begin{array}{cccc} \Sigma_{\rho}^{LP}(\sigma_p, -1, -1) & \Sigma_{\rho}^{LP}(\sigma_p, -1, 0) & \Sigma_{\rho}^{LP}(\sigma_p, -1, +1) & 0 \\ \Sigma_{\rho}^{LP}(\sigma_p, 0, -1) & \Sigma_{\rho}^{LP}(\sigma_p, 0, 0) & \Sigma_{\rho}^{LP}(\sigma_p, 0, +1) & 0 \\ \Sigma_{\rho}^{LP}(\sigma_p, +1, -1) & \Sigma_{\rho}^{LP}(\sigma_p, +1, 0) & \Sigma_{\rho}^{LP}(\sigma_p, +1, +1) & 0 \\ 0 & 0 & 0 & \Sigma_G^{LP}(\sigma) \end{array} \right)_{ji} & \text{otherwise} \end{array} \right. \quad (2.25)$$

Explicit formulas for the self-energy terms in finite volume read, with quantities defined in the isobar rest frame (superscript  $\star$ , not to be confused with complex conjugation  $*$ ),

$$\Sigma_{\rho}^{LP}(\sigma, \lambda', \lambda) = \frac{1}{2} \frac{J_P}{L^3} \sum_{\mathbf{k} \in \mathcal{S}_L} \left( \frac{\sigma}{4E_{k^*}^2} \right)^2 \frac{(-2k_{\mu}^* \epsilon_{\lambda'}^{\star\mu*}) (-2k_{\nu}^* \epsilon_{\lambda}^{\star\nu})}{E_{k^*}(\sigma - 4E_{k^*}^2)}, \quad (2.26)$$

$$\Sigma_G^{LP}(\sigma) = \frac{J_P}{L^3} \sum_{\mathbf{k} \in \mathcal{S}_L} \left( \frac{\sigma}{4E_{k^*}^2} \right)^2 \frac{1}{2E_{k^*}(\sigma - 4E_{k^*}^2)}, \quad (2.27)$$

whereas those in infinite volume are quoted in Eq. (2.21) and the  $\epsilon^*$  can be found in Ref. [16]. We checked that the difference between the finite- and infinite-volume expression at the matching points  $\text{Reg}$  are exponentially suppressed in  $m_{\pi}L$ . For an illustration of the difference between a finite and an infinite-volume quantity below threshold see the brown and dashed green lines in Fig. 8.

The two-body  $K$ -matrix provides the first part of the physical input. It is defined again in two different regimes

$$[\tilde{K}(s)^{-1}]_{(\mathbf{p}',j)(\mathbf{p},i)} = \delta_{\mathbf{p}'\mathbf{p}} \delta_{ji} \left\{ \begin{array}{ll} \tilde{K}_j^{-1}(\sigma_p) & \text{for } \sigma_p \geq \sigma_0, \\ \tilde{K}_j^{-1}(\sigma_0) & \text{otherwise.} \end{array} \right. \quad (2.28)$$

The introduction of the matching point  $\sigma_0$  is a manifestation of the fact that in the three-body sector, the third particle (spectator) can formally carry away arbitrarily high momenta  $p \in [0, \infty)$  even though there is a maximal physical spectator momentum. Thus, the three-body equation depends explicitly on the  $K$ -matrix in the unphysical (with respect to the corresponding two-body) energies  $\sigma_p \in (-\infty, 4m_{\pi}^2)$ . See Fig. 1 for a representation of the phase-space for the relevant scenarios. The question of how to fix the two-body input in this unphysical region seems to have an answer through a case-by-case decision. For example, in some purely data-driven studies [10] some features of the  $\pi\pi$  amplitude below the two-body threshold such as the Adler zero could be extracted. Here, we chose to include the pertinent phase-shift from the Inverse Amplitude Method [108] with parameters obtained from the finite-volume two-body analysis with respect to the same lattice ensembles as the one employed here, see Sect. III A. After performing pilot studies we see that for the  $I = 2 \pi\rho/\pi G$  system the influence of the  $K$ -matrix in the unphysical region (see Fig. 4) is a minor effect and choose, thus,  $\sigma_0 = 4m_{\pi}^2$ . Another smooth matching procedure is chosen in recent studies [19, 21]. Finally we also note that, since the infinite-volume equation is solved by a deformation of the complex contour in Eq. (2.11) one has to bend the contour back to real values of spectator momenta  $q_0 < q < \Lambda$  for  $q_0$  defined by  $\sigma(s, q_0) = \sigma_0$  because contour deformation is forbidden across the non-analyticity introduced by the matching.

The second part of the physical input is provided through the three-body force encoded in the FVU-formalism through the isobar-spectator interaction term  $\tilde{C}$ . In terms of  $\tilde{C}_{L'L}$  defined in the  $JLS$  basis  $\{(\pi\rho)_S, (\pi G)_P, (\pi\rho)_D\}$ ,

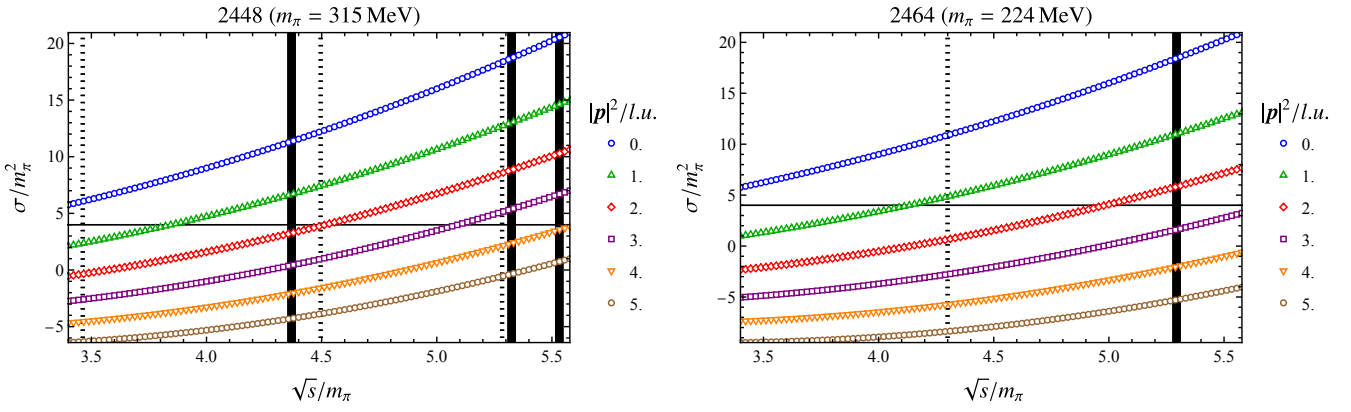


Figure 1. Kinematical coverage of the considered heavy (left panel) and light pion mass (right panel) finite-volume setups. Notation:  $\mathbf{p}$  – three-momentum of the spectator; Full horizontal line – physical two-body threshold of the two-body cluster; Thick vertical lines –  $\pi\pi\pi$  non-interacting levels; Dotted vertical lines –  $\pi\rho$  pseudo-non-interacting levels.

the contact term in helicity basis reads

$$[\tilde{C}(s)]_{(\mathbf{p}',j)(\mathbf{p},i)} = \frac{3}{4\pi} \sum_{M=-1}^1 \mathfrak{D}_{-M-\lambda(j)}^{1*}(\phi_{-\mathbf{p}'}, \theta_{-\mathbf{p}'}, 0) \tilde{C}_{ji}(s, \mathbf{p}', \mathbf{p}) \mathfrak{D}_{-M-\lambda(i)}^1(\phi_{-\mathbf{p}}, \theta_{-\mathbf{p}}, 0) \quad (2.29)$$

$$\text{with } \tilde{C}_{ji}(s, \mathbf{p}', \mathbf{p}) = U_{jL'} \tilde{C}_{L'L}(s, \mathbf{p}', \mathbf{p}) U_{Li} \quad \text{for } U_{Lj} = \begin{pmatrix} \frac{1}{\sqrt{3}} & \frac{1}{\sqrt{3}} & \frac{1}{\sqrt{3}} & 0 \\ 0 & 0 & 0 & 1 \\ \frac{1}{\sqrt{6}} & -\sqrt{\frac{2}{3}} & \frac{1}{\sqrt{6}} & 0 \end{pmatrix}_{Lj} \quad (2.30)$$

$$\text{with } \tilde{C}_{L'L}(s, \mathbf{p}', \mathbf{p}) = \sum_{k=0}^{\infty} \left( \frac{\mathbf{p}'}{m_\pi} \right)^{L'} \tilde{c}_{L'L}^k s^k \left( \frac{\mathbf{p}}{m_\pi} \right)^L \quad \text{for } \tilde{c}^k \in \mathbb{R} \quad (2.31)$$

The latter definition finalizes the set of equations needed to determine the finite-volume spectrum for a given set of two-body phase-shifts and constants  $\tilde{c}_{L'L}$ .

The remaining question is the cutoff-dependence of the quantization condition Eq. (2.23) which, so far, has only hard cutoffs, i.e., fixed by choosing the size of the matrix  $T_\Gamma$ . For easier reference, we also define “shells” referring to all points on a cubic lattice which can be related to one another through the  $O_h$ . We refer to: shell  $i = 1$  as momentum  $\mathbf{p} = (0, 0, 0)$ ; shell  $i = 2$  as the six momenta with  $|\mathbf{p}| = 2\pi/L$ ; shell  $i = 3$  as the 12 momenta with  $|\mathbf{p}| = 2\sqrt{2}\pi/L$  and so on, see also Ref. [111]. In this work, we usually consider momenta up to shell 3 ( $\Lambda = \Lambda_3 := 2\sqrt{2}\pi/L$ ) or 4 ( $\Lambda = \Lambda_4 := 2\sqrt{3}\pi/L$ ). We emphasize that: (1) the actual finite-volume calculations in this study do not rely on shells but use as the basis the momentum space of ordered three-momenta, e.g., 19 momenta for  $\Lambda_3$ ; (2) we only have to consider the cutoff in spectator momenta, not the summation in the self energy, because the self energies have been made convergent by subtraction.

The unavoidable appearance of the cutoffs in the intermediate steps of the three-particle formalisms requires a special look. Clearly, in continuum Quantum field theory any observable quantity must be independent of the choice of the cutoffs. In finite-volume formalism, energy eigenvalues are determined through the Quantization Condition Eq. (2.23). The change of the hard cutoff in spectator momentum will certainly change the size of the matrix in Eq. (2.23) and, thus, change the position of the predicted energy eigenvalues. To study this quantitatively, we concentrate on the example of the ground state energy  $E_0$  for the heavy pion mass ensemble (2448). Specifically, for fixed parameters  $\tilde{c}_{L'L}$  and fixed two-body input we determine the ground state level via Eq. (2.23) for different maximal spectator momenta  $i_{max} \in \{2, 3, 4\}$  in lattice units. Then we determine the difference for two different  $i_{max,1}$  and  $i_{max,2}$ :

$$E_0^{i_{max,1}}(m_\pi L) - E_0^{i_{max,2}}(m_\pi L). \quad (2.32)$$

The result is shown in the left panel of Fig. 2, which shows slower than exponential behavior with  $m_\pi L$ .

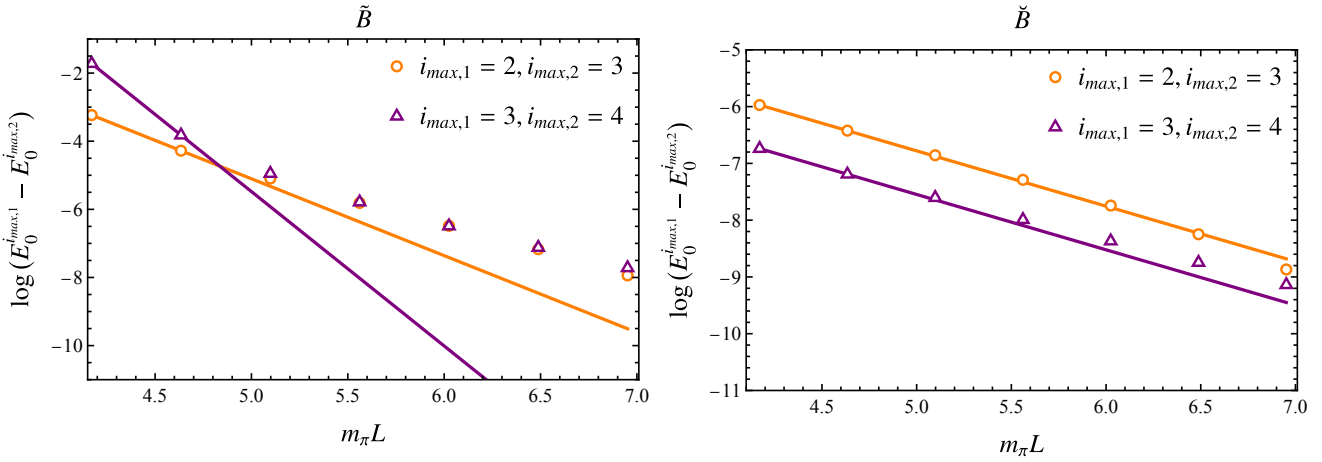


Figure 2. Cutoff dependence test between method 1 (left panel) and method 2 (right panel). In both figures the ground state level is predicted with no three-body force using a hard cutoff  $i_{max} \in \{2, 3, 4\}$ . Solid lines linearly connect the first and second values to guide to the eye.

To improve this behavior one can add a smooth form factor [26, 46]. Here we follow a slightly different path and subtract the one-particle exchange term, which leads to suppression of large momenta without spoiling unitarity. For this we start with the discontinuity of a generic  $B$ -term, following Ref. [104] adapted to the current notation and convention,

$$\text{Disc } B(\sqrt{s}) = -2\pi i \frac{\delta(\sqrt{s} - \sqrt{s_{\text{on}}})}{2E_{p+p'}} N, \quad (2.33)$$

with  $\sqrt{s_{\text{on}}} := E_p + E_{p'} + E_{p+p'}$  and  $N$  a non-singular numerator depending on momenta, scattering angles, and energy. Note the minus sign owing to the different convention of the  $S$ -matrix in the current work compared to Ref. [104]. Dispersing in  $\sqrt{s}$  one obtains

$$B(\sqrt{s}) = \frac{1}{2\pi i} \int_{3m}^{\infty} d\bar{W} \frac{\text{Disc } B(\bar{W})}{\bar{W} - \sqrt{s} - i\epsilon} = \frac{N}{2E_{p+p'}} \frac{1}{\sqrt{s} - \sqrt{s_{\text{on}}} + i\epsilon}, \quad (2.34)$$

which has, indeed, the exact denominator structure of Eq. (2.3). One can repeat this exercise with two subtractions in  $\sqrt{s}$ , leading to:

$$B(\sqrt{s}) = B(0) + B'(0)\sqrt{s} + \frac{s}{s_{\text{on}}} \frac{N}{2E_{p+p'}} \frac{1}{\sqrt{s} - \sqrt{s_{\text{on}}} + i\epsilon}. \quad (2.35)$$

The first two terms can be absorbed in fit parameters. Inserting helicities, isospin, and momentum dependence for the second term, we obtain

$$\check{B}_{\lambda' \lambda}(s, \mathbf{p}', \mathbf{p}) = \frac{s}{s_{\text{on}}} \tilde{B}_{\lambda' \lambda}(s, \mathbf{p}', \mathbf{p}) \quad (2.36)$$

with  $\tilde{B}$  from Eq. (2.3). These subtractions ensure a stronger suppression for large spectator momenta without changing the one-particle exchange term at the (three-particle) onshell point ( $s = s_{\text{on}}$ ), i.e., without spoiling three-body unitarity. The three-body force term  $\tilde{C}$  depends also on the spectator momenta. Since it is not fixed from unitarity it can be simply regulated with a form-factor, to obtain a similar suppression of large momenta as the  $\check{B}$ -term,

$$\check{C}_{L'L}(s, p', p) = F_{L'}(p') \left( \frac{p'}{m_\pi} \right)^{L'} \check{c}_{L'L}(s) \left( \frac{p}{m_\pi} \right)^L F_L(p), \quad F_L(p) = \left( \frac{\check{\Lambda}^2}{\check{\Lambda}^2 + p^2} \right)^{L+1}. \quad (2.37)$$

This leads to a modified quantization condition,

$$\text{Method 2: } \sqrt{s} \in \{E_0, E_1, \dots\}^\Gamma \iff \left\langle E_L \left[ (\tilde{K}^{-1}(s) - \Sigma^{FV}(s)) E_L - (\check{B}(s) + \check{C}(s)) \right]^{-1} E_L \right\rangle_\Gamma = \infty. \quad (2.38)$$

Repeating the previous test which leads to the result depicted in the right panel of Fig. 2. Indeed, the jumps of the predicted ground state finite-volume level due to the increased cutoff show much milder (close to exponentially suppressed) behavior in  $m_\pi L$ .

In summary, we derive two types of the three-body quantization conditions for the  $I = 2 \pi\pi\pi$  system extending the finite volume unitarity framework [32, 46] through a coupled-channel  $\pi\rho/\pi G$  system. Both methods have their respective areas of application, i.e., method 1 maintains closer connection to diagrams derivable from some microscopic (Lagrangian) theory, while method 2 can be considered as a more controlled way to extract the infinite-volume information from a given finite-volume spectrum directly. Both methods will be utilized below.

### III. LATTICE QCD SPECTRUM

#### A. Lattice QCD setup

The finite-volume energy spectrum can be accessed through two-point correlation functions in the lattice QCD framework, see, e.g., Refs. [1, 112, 113] for reviews. This is done by calculating the time dependence of the correlation function of operators  $\mathcal{O}_i$  which create/annihilate the states of interest,

$$C_{ij}(t) = \left\langle \mathcal{O}_i(t) \mathcal{O}_j^\dagger(0) \right\rangle = \sum_n \langle 0 | \mathcal{O}_i | n \rangle \langle n | \mathcal{O}_j^\dagger | 0 \rangle e^{-E_n t}. \quad (3.1)$$

If the operators are constructed with definite quantum numbers matching the states of interest, the only contributions to the above sum will come from states  $n$  with the same quantum numbers. The energies  $E_n$  can then be extracted by measuring the correlation function on an ensemble and fitting the temporal behavior. To better determine the excited-state spectrum we use a variational analysis [114–116] on a basis of several different operators. In this work we perform all calculations on the two cubic ensembles from the GWQCD collaboration detailed in Table I. These ensembles were generated using  $N_f = 2$  quarks with an nHYP-smeared clover action. Details of the determination of the mass and decay constant for the pion and kaon can be found in Ref. [12]. Valence quarks that appear in operators are treated using all-to-all LapH perambulators [117] computed using our optimized inverter [118].

Due to the calculations being performed in a cubic volume the  $SO(3)$  symmetry found in nature is reduced to the cubic symmetry group  $G = O_h$ . Our operators must then be constructed to have overlaps with states  $n$  labeled by the irreducible representations (irreps),  $\Lambda$ , of  $O_h$  instead of angular momentum. For this study of  $\pi\rho$  scattering with  $I = 2$ , we are interested in the  $T_{1g}$  irrep to complement our results on the  $a_1(1260)$  [16]. In this irrep the lowest infinite volume quantum numbers that appear are  $J^P = 1^+$ . Our operator basis is then constructed out of two types,  $\rho\pi$  and  $\pi\pi\pi$ . First we construct operators to have definite isospin  $I = 2$  and we choose  $I_3 = 2$  which is arbitrary in

Table I. Details of the GWQCD  $N_f = 2$  ensemble parameters used in this work. Here,  $a$  is the lattice spacing,  $N_{\text{cfg}}$  the number of Monte-Carlo configurations for each ensemble. The pion and kaon masses are  $aM_\pi$  and  $aM_K$ , respectively. The errors on every value are purely stochastic except the lattice spacing which includes an estimated 2% systematic uncertainty.

Ensemble	$N_t \times N^3$	$a/\text{fm}$	$N_{\text{cfg}}$	$aM_\pi$	$af_\pi$	$aM_K$	$af_K$
2448	$48 \times 24^3$	0.1210(2)(24)	300	0.1931(4)	0.0648(8)	0.3236(3)	0.1015(2)
2464	$64 \times 24^3$	0.1215(3)(24)	400	0.1378(6)	0.0600(10)	0.3132(3)	0.0980(2)

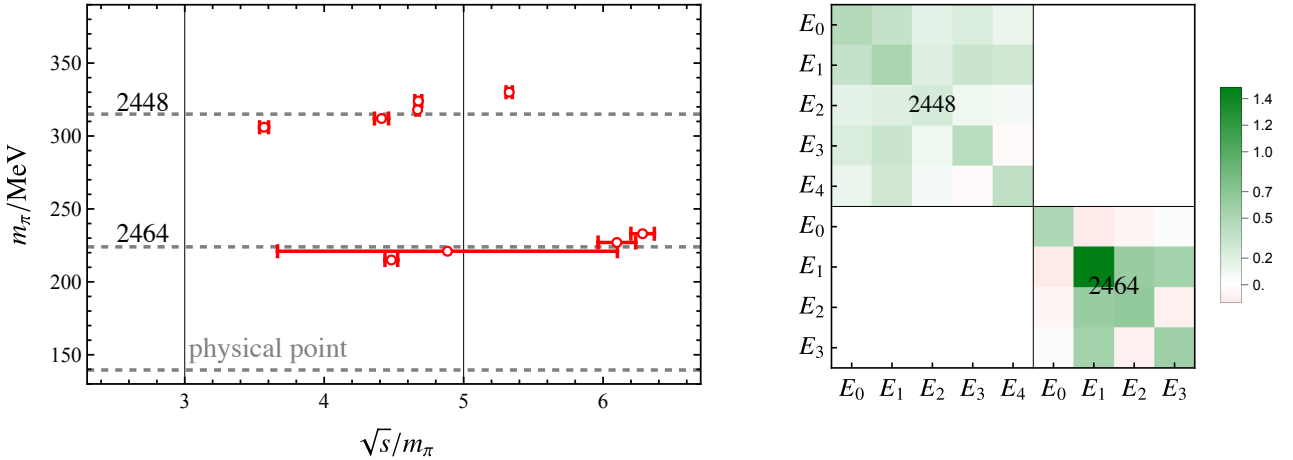


Figure 3. Summary of the lattice results for ensembles in Tab. I. Left panel: Overview of the finite-volume lattice spectrum with respect to the relevant thresholds and pion mass values. Error bars represent a combination of statistical and systematic error from model averaging. Right panel: Covariance matrix of the pertinent results.

$N_f = 2$  simulations, these are

$$\begin{aligned} \rho(\mathbf{p}_\rho)\pi(\mathbf{p}_\pi) &= \rho^+(\mathbf{p}_\rho)\pi^+(\mathbf{p}_\pi), \\ \pi\pi\pi_1(\mathbf{p}_1, \mathbf{p}_2, \mathbf{p}_3) &= \frac{\sqrt{2}}{2} [\pi^+(\mathbf{p}_1)\pi^0(\mathbf{p}_2)\pi^+(\mathbf{p}_3) - \pi^0(\mathbf{p}_1)\pi^+(\mathbf{p}_2)\pi^+(\mathbf{p}_3)], \\ \pi\pi\pi_2(\mathbf{p}_1, \mathbf{p}_2, \mathbf{p}_3) &= \frac{\sqrt{6}}{3} \left[ \pi^+(\mathbf{p}_1)\pi^+(\mathbf{p}_2)\pi^0(\mathbf{p}_3) - \frac{1}{2}\pi^+(\mathbf{p}_1)\pi^0(\mathbf{p}_2)\pi^+(\mathbf{p}_3) - \frac{1}{2}\pi^0(\mathbf{p}_1)\pi^+(\mathbf{p}_2)\pi^+(\mathbf{p}_3) \right]. \end{aligned} \quad (3.2)$$

The above operators are then projected onto an irrep of  $O_h$  using the formulas

$$\begin{aligned} \mathcal{O}_{\rho_i\pi}^{\Lambda,\mu}(\mathbf{p}_\rho, \mathbf{p}_\pi) &= \frac{n_\Lambda}{|G|} \sum_{g \in G} U_{\mu\mu}^\Lambda(g) \det[R_g] (R_g)_{ij} \rho_j(R_g \mathbf{p}_\rho) \pi(R_g \mathbf{p}_\pi), \\ \mathcal{O}_{(\pi\pi\pi)}^{\Lambda,\mu}(\mathbf{p}_1, \mathbf{p}_2, \mathbf{p}_3) &= \frac{n_\Lambda}{|G|} \sum_{g \in G} U_{\mu\mu}^\Lambda(g) \det[R_g] \pi(R_g \mathbf{p}_1) \pi(R_g \mathbf{p}_2) \pi(R_g \mathbf{p}_3). \end{aligned} \quad (3.3)$$

Here  $\mu$  is a row of the irrep  $\Lambda$ ,  $n_\Lambda$  is the dimension of the irrep, for each group element  $g$ ,  $U$  is the representation matrix in the irrep  $\Lambda$  and  $R$  the three-dimensional rotation for the element. The same finite-volume projector is used for both three-pion isospin combinations because the isospin and finite-volume rotations are independent of each other. The above cubic group projectors are applied to all the definite isospin constructions for all momenta combinations that have a non-interacting energy below or slightly above the next inelastic threshold.

Once the correlation functions are computed on the GWQCD ensembles, we must apply the variational method and fit the eigenvalues to extract the energies. The usual GWQCD procedure is to choose a set of fitting parameters that produce a result which is stable under small changes of these parameters and report a statistical error bar. In this work we use model averaging [119, 120] to improve our error estimates. The procedure is to perform a  $\chi^2$  minimization on many different sets of fitting parameters. Data from all of these fits are used to then compute an average over all of the models, giving errors that include statistical and systematic uncertainties. To ensure the models included in the averaging are reasonable representations of the data, we make quality cuts if the model probability is extremely small or if the statistical error on the mass is larger than  $0.5 m_\pi$ . The resulting finite-volume spectrum and covariance

matrices resulting from model averaging are depicted for both ensembles in Fig. 3 and read

$$E_{2448}/m_\pi = \begin{pmatrix} 3.56901 \\ 4.41120 \\ 4.66988 \\ 4.67493 \\ 5.32662 \end{pmatrix}, \quad \Sigma_{2448}/m_\pi^2 \cdot 10^3 = \begin{pmatrix} +1.01877 & +0.26637 & +0.08848 & +0.15485 & +0.06649 \\ +0.26637 & +2.53427 & +0.1188 & +0.26144 & +0.1986 \\ +0.08848 & +0.11880 & +0.1563 & +0.06604 & +0.06259 \\ +0.15485 & +0.26144 & +0.06604 & +0.62033 & -0.01832 \\ +0.06649 & +0.1986 & +0.06259 & -0.01832 & +0.50127 \end{pmatrix},$$

$$E_{2464}/m_\pi = \begin{pmatrix} 4.48159 \\ 4.88395 \\ 6.09908 \\ 6.28352 \end{pmatrix}, \quad \Sigma_{2464}/m_\pi^2 \cdot 10^3 = \begin{pmatrix} +2.07964 & -9.31646 & -0.35639 & +0.03441 \\ -9.31646 & +1484.79 & +8.25206 & +6.25899 \\ -0.35639 & +8.25206 & +18.1982 & -0.86329 \\ +0.03441 & +6.25899 & -0.86329 & +7.07176 \end{pmatrix}, \quad (3.4)$$

with finite-volume energy eigenvalues  $E_{\text{ens}}$  and the covariance matrices  $\Sigma_{\text{ens}}$  of heavy ( $m_\pi \approx 315$  MeV) and light ( $m_\pi \approx 224$  MeV) ensembles as denoted in Tab. I.

## B. Fits to lattice finite-volume spectrum

We determine the parameters of the three-body scattering amplitude by fitting them to the LQCD data of Eq. (3.4) using the quantization condition (QC) of method 2 of Eq. (2.38). The lattice results presented in Sect. III A are available for two different scenarios:  $m_\pi \sim 224$  MeV ( $m_\pi L \sim 3.30$ ) and  $m_\pi \sim 315$  MeV ( $m_\pi L \sim 4.63$ ), both for the cubic box in the  $\Gamma = T_{1g}$  irrep. As summarized in Fig. 3 the heavy pion mass (2448) results are more precise and numerous in the elastic region and we concentrate our analysis on them. All results in the following refer to this ensemble unless specified otherwise. Comparing these results with the kinematics shown in Fig. 1 we note that at least 3 spectator momentum shells are needed to cover the physical two-body dynamics in the subsystem of the three-body system, in the elastic window for  $3m_\pi < \sqrt{s} < 5m_\pi$ . This defines the intrinsic cutoff of our calculation to  $\Lambda_3 = 2\pi/L \cdot \sqrt{2} \approx 1.91 m_\pi$ . To study the cutoff dependence we will also consider 4 shells, corresponding to  $\Lambda_4 = 2\pi/L \cdot \sqrt{3} \approx 2.35 m_\pi$ .

On one hand, the input of the QC consists of the  $\pi\pi$  phase-shifts  $\delta^{11}$  and  $\delta^{20}$  in Eq. (2.21). In the present study, we take this information from the best fit to the  $\pi\pi$  energy eigenvalues for all possible isospin combinations calculated on the same and other ensembles [109]. The other input to the quantization condition is the three-body force  $\check{C}$  in Eq. (2.37). In general, this real-valued term is energy and spectator-momentum dependent. For the latter we chose a smooth cutoff of  $\check{\Lambda} = 2 m_\pi$ .

In addition, there are six independent channel transitions. With four data points available in the elastic window, we try different two- and three-parameter strategies. They are shown in Table II, quoting only the central values. We have also tried to perform fits with additional energy dependence, but the data are too few and not precise enough to make meaningful statements. We also note that we cannot fit the heavy pion mass data with  $\check{c}_{00}$  alone. One of the reasons is the occurrence of two data points at almost the same energy at  $\sqrt{s} \approx 4.7 m_\pi$ . This is a clear sign that  $S$ -wave  $\pi\rho$  dynamics alone cannot explain the LQCD spectrum.

For most of the fits (1,2,4,7) we chose a factorization of the contact term

$$\check{c}_{00} = g_S^2, \check{c}_{22} = g_D^2, \check{c}_{02} = g_D g_S, \check{c}_{01} = g_S g_P, \check{c}_{11} = g_P^2, \check{c}_{12} = g_P g_D ,$$

minimizing the number of parameters. Fit 3 has one parameter for each term  $\check{c}_{00}$ ,  $\check{c}_{02}$ , and  $\check{c}_{22}$ , but the fit values stay close to the ones using factorization (fit 1).

We observe that fits 1 and 2 (that is fitting  $g_S$  and  $g_D$  only) already leads to a good description of the spectrum. In the following we explore these two fits in more detail. The respective best fit values, their uncertainties and their

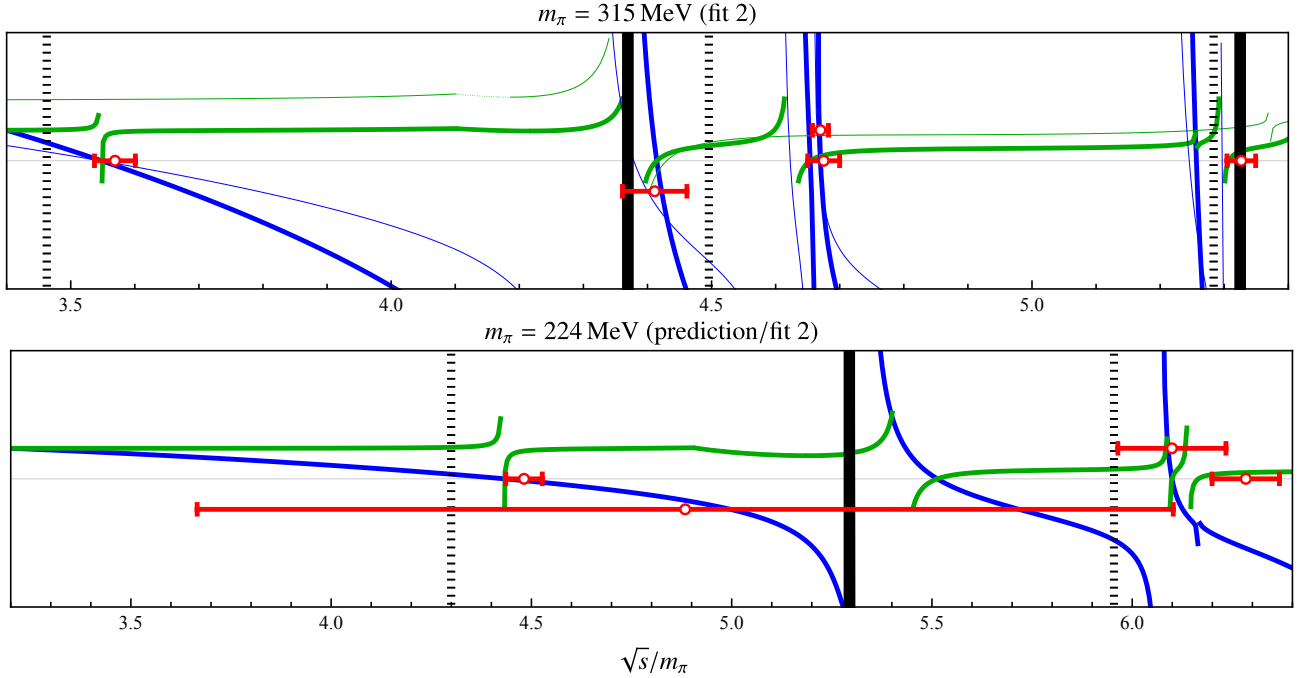


Figure 4. Example of the level determination through the FVU approach. Top panel: Fit 2 (see Tab. II using method 2 (2.38)) to the heavy pion mass lattice QCD spectrum (open symbols) for  $\sqrt{s} < 5 m_\pi$  and using. Energy eigenvalues correspond to the zeros (vertical orange lines) of  $T_{T_{1g}}^{-1}$  (green/blue lines). Thin green/blue lines denote the same quantity but for turned off inter-channel coupling. Lower panel: Prediction of the light-pion mass spectrum using fit 2 parameters. In both plots the thick solid (dashed) vertical lines denote non-interacting levels of the  $3\pi(\pi\rho)$  system.

correlations, obtained from re-sampling the correlated LQCD data read

$$\begin{aligned} \text{Fit 1 } (i_{\max} = 3) : \quad & \begin{pmatrix} g_S \\ g_D \end{pmatrix} = \begin{pmatrix} 4.929 \\ 2.063 \end{pmatrix}, \quad \Sigma_{\text{Fit 1}} \cdot 10^3 = \begin{pmatrix} 1.1 & 0.40 \\ 0.40 & 0.15 \end{pmatrix}, \\ \text{Fit 2 } (i_{\max} = 4) : \quad & \begin{pmatrix} g_S \\ g_D \end{pmatrix} = \begin{pmatrix} 5.377 \\ 2.296 \end{pmatrix}, \quad \Sigma_{\text{Fit 2}} \cdot 10^3 = \begin{pmatrix} 1.9 & 0.73 \\ 0.73 & 0.29 \end{pmatrix}. \end{aligned} \quad (3.5)$$

The comparison of the fitted levels with the LQCD ones is shown in Fig. 4 for fit 2. As a technical aspect, we found that using multiple matrix elements – hereby  $\pi\rho(0)$  denoting the  $\pi\rho \rightarrow \pi\rho$  transition for momenta on the first shell and  $\pi G(1)$  denoting  $\pi G \rightarrow \pi G$  the transition on the second shell projected to the relevant irrep  $\Gamma = T_{1g}$  – stabilizes the search for the roots of  $T_\Gamma^{-1}$  significantly. Furthermore, this gives access to additional information, namely the dominant channel for each individual interacting energy eigenvalue. For example, for the ground state level  $E_0 \approx 3.57$  we clearly observe that the  $\pi\rho$  channel is dominant. This is in line with the finding shown in Fig. 6 that removing the  $\pi G$  channels barely changes the value of  $E_0$ .

To study the channel dynamics further, we turn off the inter-channel coupling (off-diagonal elements in  $\check{B}$  and  $\check{C}$  for fixed diagonal elements of the three-body force  $\check{C}$ ). The resulting  $T_{T_{1g}}^{-1}$  are shown with the thin green/blue lines in Fig. 4. Indeed, we observe that in this *unphysical* show-case scenario only the  $\pi\rho$  channel has a zero transition at  $E_0$ . This also makes sense from the point of view of the nearby presence of the pseudo- $\pi\rho$  non-interacting level, assuming a stable  $\rho$ -meson with the mass provided by  $\delta_{11} = \pi/2$ , i.e.,  $m_\rho \approx 2.46 m_\pi$ . Apparently, the much weaker interaction in the  $\pi G$  channel only leads to small corrections which has already been discussed for Fig. 6. Naturally, the interpretation of the dominant mechanism becomes harder with higher energies. For  $E_1 \approx 4.41 m_\pi$  we observe that the  $T_{T_{1g}}^{-1}$  for both decoupled  $\pi G$  and  $\pi\rho$  channels have zeros, while for the next two levels, again, the  $\pi\rho$  channel dominates.

To be more specific, we define a quantitative measure for the importance of  $\pi\rho$  vs.  $\pi G$  channel as the absolute value of the residuum of  $T_{T_{1g}}(\sqrt{s} = E_i)$  for the respective energy eigenvalue and in each of the final isobar-spectator states. This leads to the result depicted in Fig. 5 where we restrict the discussion to the spectator momentum zero for the  $\pi\rho$  state,  $\pi\rho(0)$  ( $\pi\rho \rightarrow \pi\rho$  transition with all states at rest), and the  $\pi G(1)$  state ( $\pi G \rightarrow \pi G$  transition with back-to-back momenta of magnitude 1 in lattice units). Taking the result at face value, e.g., without addressing the question if

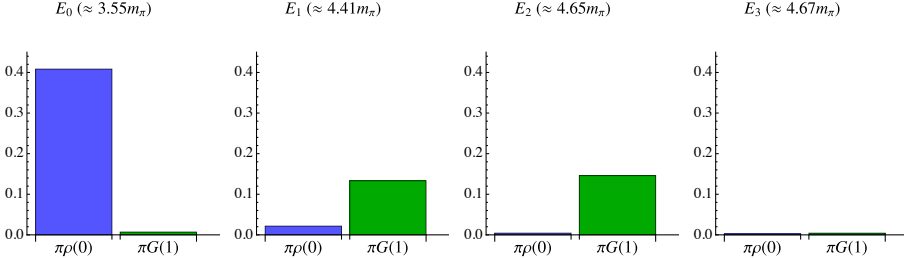


Figure 5. Residua of the determined finite-volume energy eigenvalue states for the heavy pion mass setup (fit 2). Residua are compared between the  $\pi\rho \rightarrow \pi\rho$  state of zero momenta ( $\pi\rho(0)$ ) with the  $\pi G \rightarrow \pi G$  state with back-to-back momenta of magnitude 1 in lattice units ( $\pi G(1)$ ).

residues are measurable, we observe that  $E_0$  is mostly dominated by the  $\pi\rho$  state. The residues reveal that the first excited state,  $E_1$ , has a considerable  $\pi G$  admixture, but it should also be noted that the  $\rho$  meson has a finite momentum at  $E_1$ , i.e., the considered  $\pi\rho(0)$  state is off-shell, rendering its residue small without the amplitude necessarily being small. Indeed, we note that the highest-energy eigenvalue overlaps very weakly with both the  $\pi\rho(0)$  and  $\pi G(1)$  states, which indicates the importance of higher-momentum states. Our observation seems to be independent of the chosen cutoff. Extending on this pilot investigation, one can think of using these states on higher shells and then determining residua of individual channels. It is then tempting to think that such a decomposition could be compared to the operator overlap of individual plateaus, providing another input for the three-body quantization conditions.

As a further remark we also observe that even outside of the range of validity of the quantization condition ( $\sqrt{s} > 5m_\pi$ ) one predicted level (see Fig. 4) overlaps with that from the lattice QCD determination within  $\approx 1\sigma$ . This suggests that  $5\pi$  interactions are rather sub-leading to those of three pions. Finally, assuming that the obtained three-body force  $\tilde{C}$  does not change with the pion mass, but changing the two-body input as demanded by the IAM implementation, we can predict the finite-volume spectrum for the 2464 ensemble, see Fig. 4. We observe agreement ( $\chi^2/\text{dof} \sim 1$ ) of our prediction with the available finite-volume spectrum, but note large uncertainties on the latter.

Table II. Fit results (method 2) to all lattice QCD data in the elastic window, see Fig. 3. Different values of  $i_{\text{max}}$  correspond to different cutoffs  $\Lambda$ . Note that, for a confidence level of  $\alpha = 20\%$ , only those fits are shown that cannot be rejected due to their  $\chi^2$ , i.e., if  $0.2 < \chi^2 < 4.6$  for  $\text{dof}=2$  and  $0.02 < \chi^2 < 2.7$  for  $\text{dof}=1$ .

Fit	$m_\pi$	$i_{\text{max}}$	$\chi^2/\text{dof}$	$\check{c}_{00}$	$\check{c}_{02}$	$\check{c}_{22}$	$\check{c}_{01} \cdot m_\pi$	$\check{c}_{11} \cdot m_\pi^2$	$\check{c}_{12} \cdot m_\pi$
1	315	3	$1.86/(4-2) = 0.93$	24.3	10.2	4.3	-	-	-
2	315	4	$1.98/(4-2) = 0.99$	28.9	12.3	5.3	-	-	-
3	315	3	$0.30/(4-3) = 0.30$	26.7	10.2	7.5	-	-	-
4	315	3	$1.68/(4-2) = 0.84$	12.4	-	-	13.4	14.5	-
6	315	4	$0.42/(4-3) = 0.42$	27.4	10.1	7.5	-	-	-
7	315	4	$1.48/(4-2) = 0.74$	12.3	-	-	13.4	14.5	-
9	224	3	$0.26/(2-1) = 0.26$	33.8	-	-	-	-	-

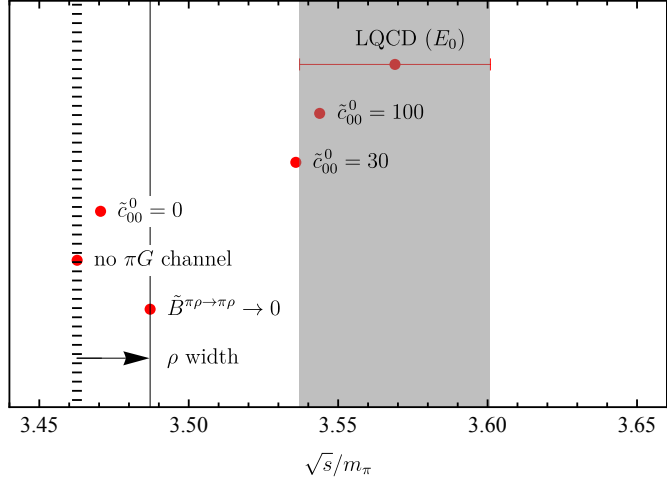


Figure 6. Different contributions to the ground state energy eigenvalue for the heavy pion mass using method 1 (unsubtracted  $\tilde{B}$ , no form factor for  $\tilde{C}$ ), for  $\Lambda = \Lambda_3$  (third shell). All  $\tilde{c}_{L'L}^{(k)} = 0$  except for  $\tilde{c}_{00}^0$ , i.e.,  $\tilde{C}_{00} = \tilde{c}_{00}^0$ . The dashed vertical line shows the infinite-volume  $\pi\rho$  “threshold” defined as  $\sqrt{s} = m_\pi + m_\rho$  such from the condition  $\{\sqrt{\sigma} = m_\rho | \cot \delta^{11}(\sqrt{\sigma}) = 0\}$ . The thin vertical line, showing the finite-volume energy without any interactions between  $\pi$  and  $\rho$ , is shifted to higher energies due to the small but finite width of the  $\rho$ -meson. See text for further explanations.

#### IV. COUPLED-CHANNEL DYNAMICS

In this section we discuss qualitative aspects of the coupled-channel system, mostly relying on method 1 (see Eq. (2.23)) to study the cut-off dependence and the influence of individual channels, as well as the limit of a narrow  $\rho$  and a comparison with an effective  $\pi\rho$  interaction. Fits to lattice energies and infinite-volume mappings are carried out in Sec. V using method 2 (see Eq. (2.38)).

##### A. Dynamics at the $\pi\rho$ threshold

First, we turn our attention to the ground state level  $E_0$  determined in various scenarios of method 1 of Eq. (2.23) for the heavy pion mass with a summary plot in Fig. 6. From top to bottom, we note that the energy eigenvalue determined from method 1 is inside the  $1\sigma$  band of the LQCD calculation for a choice of the contact term of Eq. (2.31),  $\tilde{c}_{00}^0 > 30$ , saturating at around  $\sqrt{s} \approx 3.548 m_\pi$  for  $\tilde{c}_{00}^0 \rightarrow \infty$ . We will come back to this particular behavior in Sec. IVB. Reducing  $\tilde{c}_{00}^0$ , the energy eigenvalue becomes smaller, i.e., the repulsion is reduced, as the case  $\tilde{c}_{00}^0 = 0$  demonstrates. If one also removes the  $\pi G$  channel (for fixed  $\tilde{c}_{00}^0 = 0$ ), the energy is further reduced, demonstrating that the  $\pi G$  channel provides a small repulsion. In addition to all these changes one can also consider the limit of vanishing  $\pi\rho \rightarrow \pi\rho$  interaction,  $\tilde{B}^{\pi\rho \rightarrow \pi\rho} \rightarrow 0$ . In that case the energy increases as shown towards the bottom of the figure, demonstrating that pion exchange leads to a small attraction in the  $I = 2$  channel. This last data point best reflects the “non-interacting” case, which is why we draw the thin, solid reference line through it. The reference point is shifted compared to the value  $\sqrt{s} = m_\pi + m_\rho$  (dashed vertical line) due to finite-volume effects. For this comparison we define  $m_\rho$  through  $\{\sqrt{\sigma} = m_\rho | \cot \delta^{11}(\sqrt{\sigma}) = 0\}$ , i.e., the two-body energy at which the  $\rho$  phase passes through  $90^\circ$ .

In summary, the  $I = 2$   $\pi\rho$  system is clearly repulsive at the  $\pi\rho$  threshold. Pion exchange in the  $\pi\rho$  channel provides a small attraction while the  $\pi G$  channel exhibits an even smaller repulsion. The observed, much larger repulsion can only be achieved by a repulsive contact term  $\tilde{C}$  whose value depends on the regularization as discussed in the next subsection.

## B. Singular behavior of the contact term

The saturation effect for  $\tilde{C}$  observed in Fig. 6 is only part of the singular behavior in  $\tilde{C}$  as shown in more detail in Fig. 7. There, the  $\tilde{c}_{00}^0$  is fitted in method 1 (see Eq. (2.23) and Eq. (2.31)) to the ground state  $E_0$  of the heavy pion mass lattice result for various values of the cutoff  $\Lambda_i$  defined through the number of included shells  $i$ . Starting at the lowest cutoff  $i = 1$ , the best fit value  $\tilde{c}_{00} \approx 17$ , growing to  $\approx 31$  when two shells are included. Interestingly, FVU with three shells fits the ground state lattice eigenvalue only if  $\tilde{c}_{00} \approx -25$ , growing thereafter again with the increasing cutoff. All numerically stable results are collected in Fig. 7, where a gray line is added to guide the eye.

To study the mechanism of this unusual behavior, it is instructive to consider only connected diagrams, i.e.,  $T_{ji}(s, \mathbf{p}', \mathbf{p})$ . Physical singularities of the finite-volume amplitude like  $E_0$  are unchanged by this because the disconnected part only cancels unphysical singularities (spurious poles) [74, 104]. To obtain a qualitative understanding we set  $\tilde{B}^{\pi\rho\rightarrow\pi\rho} = 0$  which is allowed because that term is small and smooth in the vicinity of  $E_0$ . In addition, we remove the  $\pi G$  channel, because the saturation of  $\tilde{c}_{00}^0$  observed in Fig. 6 persists without that channel. Omitting the channel index, we note that in finite volume the integral equation for the connected piece Eq. (2.2) becomes a matrix equation, the elements of which read

$$T(s, \mathbf{p}', \mathbf{p}) = \tilde{C}(s, \mathbf{p}', \mathbf{p}) + \frac{1}{L^3} \sum_{\mathbf{k} \in (2\pi/L)\mathbb{Z}^3} \tilde{C}(s, \mathbf{p}', \mathbf{k}) \frac{\tilde{\tau}(\sigma_k)}{2E_{\mathbf{k}}} T(s, \mathbf{k}, \mathbf{p}). \quad (4.1)$$

Assuming that  $\tilde{C}$  is both momentum and energy independent one gets

$$T(s) = \frac{1}{\tilde{C}^{-1} - \tilde{G}(s)}, \quad \text{for} \quad \tilde{G} = \frac{1}{L^3} \sum_{\mathbf{k} \in (2\pi/L)\mathbb{Z}^3} \frac{\tilde{\tau}(\sigma_k)}{2E_{\mathbf{k}}}, \quad (4.2)$$

Note that shell 1 ( $k = 0$ ,  $\sigma_0 = (\sqrt{s} - m_\pi)^2$ ), plays a special role because it produces a pole in  $\tilde{\tau}$  close to the observed ground state level. In the proximity of the pole of a stable  $\rho$ -meson we can approximate

$$\tilde{\tau}_0 \approx \frac{a_{-1}^{(0)}}{\sqrt{s} - (m_\pi + m_\rho)}, \quad (4.3)$$

abbreviating  $\tilde{\tau}_k := \tilde{\tau}(\sigma_k)$ , because  $\tilde{\tau}_0$  has a pole at around  $\sqrt{s} \approx m_\pi + m_\rho = 3.487 m_\pi$ , see Fig. 6. Here,  $a_{-1}^{(0)}$  is the residue, and all residua are found to be positive,  $a_{-1}^{(k)} > 0$ . Furthermore, one trivially has that  $\sqrt{\sigma_k} < \sqrt{s}$ . Consequently, for all  $k \geq 1$ ,  $\tilde{\tau}_k < 0$  at threshold,  $\sqrt{s} = m_\pi + m_\rho$ . This is then also true for the sum,  $b := \sum_{k \geq 1} \tilde{\tau}_k < 0$  at threshold. Of course, the size of  $b$  depends on the cutoff in the spectator momentum.

Note now that we evaluate  $\tilde{G}$  at the measured three-body energy level,  $E_0$ , which fulfills  $E_0 > m_\pi + m_\rho$  as Fig. 6 shows. Putting everything together, the lattice three-body energy  $E_0$  implies  $T_\Gamma(s = E_0^2) = \infty$  so that

$$0 = \tilde{C}^{-1} - \tilde{G}(E_0^2) = \tilde{C}^{-1} - \frac{a_{-1}^{(0)}}{E_0 - (m_\pi + m_\rho)} - b =: \tilde{C}^{-1} - \frac{a_{-1}^{(0)}}{\Delta E} - b \implies \tilde{C}^{-1} = \frac{a_{-1}^{(0)}}{\Delta E} + b \quad (4.4)$$

with  $\Delta E > 0$ ,  $a_{-1}^{(0)} > 0$ , and  $b < 0$  becoming more and more negative with increasing  $\Lambda$ , i.e., increasing  $i_{\max}$ . This explains why the contact term  $\tilde{C}$  can diverge. We illustrate this behavior numerically using the discussed simplification. For this, we consider the limit of a narrow isobar. For an isobar mass  $m_\rho$ , we have approximately

$$\tilde{\tau}_k \rightarrow \frac{2g_1^2}{\sigma_k - m_\rho^2 + i\epsilon} \quad (4.5)$$

as considered in the Appendix of Ref. [104]. Here,  $g_1 \approx 5.8$  calculated from Ref. [109] by using the quoted residue in combination with Eq. (3) from Ref. [121]. This value, determined from a global fit to LQCD data across different isospins, is very similar to the value determined in Ref. [122],  $g_1 \approx 5.6$ . In finite volume, one neglects the  $\epsilon$  and obtains that  $\tilde{G}$  from the quantization condition of Eq. (4.4) is replaced through Eq. (4.5) according to

$$0 = \tilde{C}^{-1} - 4\pi\tilde{G}_{\lim}^{\text{FV}} \quad \text{with} \quad \tilde{G}_{\lim}^{\text{FV}} = \frac{2g_1^2}{L^3} \sum_{\mathbf{k} \in \mathcal{S}_L} \frac{1}{4\pi} \frac{1}{2E_{\mathbf{k}}} \frac{1}{s + m_\pi^2 - 2\sqrt{s}E_{\mathbf{k}} - m_\rho^2}. \quad (4.6)$$

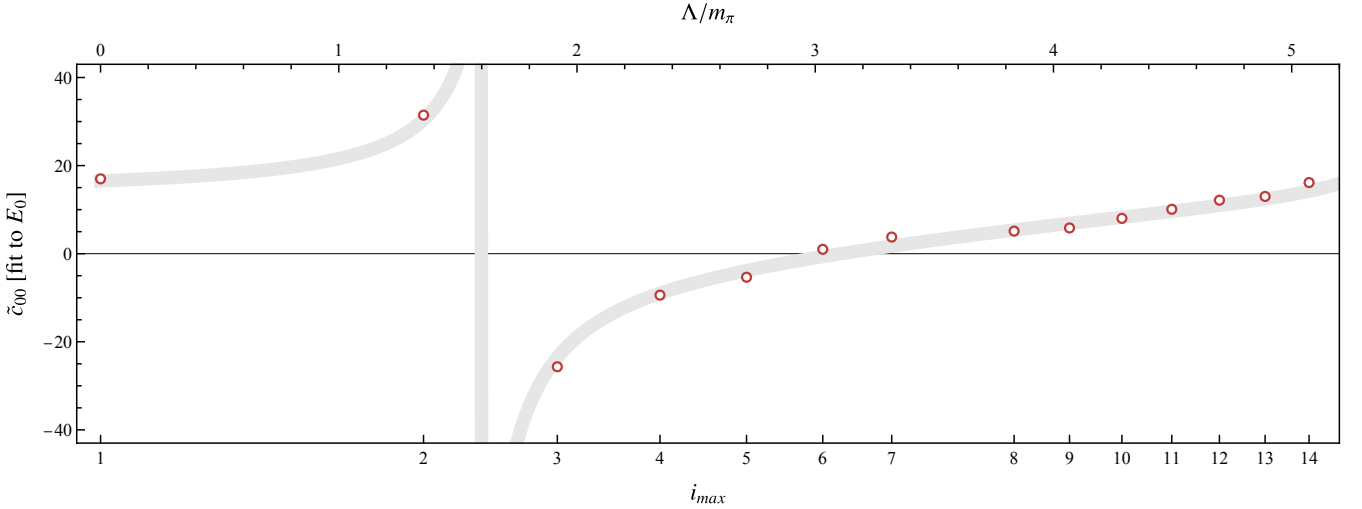


Figure 7. Best fit values of  $\tilde{c}_{00}^0$  in method 1 of the FVU quantization condition (c.f. Eq. (2.23)) fitted to the ground state energy  $E_0$  of the heavy pion mass ensemble at different cutoff values (maximal shell  $i_{max}$ ). All other coefficients ( $\tilde{c}_{L'L}^k$ ) are set to zero. The gray thick line is a crude interpolation added to guide the eye.

Note that this equation is still defined in the plane-wave basis. In light of Eq. (2.31) and Eq. (2.7), there is a factor of  $(4\pi)$  of the  $\tilde{C} = \tilde{C}_{00}/(4\pi)$  compared to the  $S$ -wave projected  $\tilde{C}_{00}$ . We will need the partial-wave  $\tilde{G}_{\text{lim}}$  in the following which is why it is introduced here with a factor of  $1/(4\pi)$ . In the infinite-volume partial-wave basis, neglecting  $\tilde{B}$  and the  $\pi G$  channel, and substituting  $\tilde{\tau}$  according to Eq. (4.5), Eq. (2.11) becomes

$$T_{00}(s) = \tilde{C}_{00}(s) + \tilde{C}_{00}(s) \tilde{G}_{\text{lim}}^{\text{IV}} \tilde{T}_{00}(s) \quad \text{where} \quad \tilde{G}_{\text{lim}}^{\text{IV}} = \int_0^{\Lambda} \frac{dl l^2}{(2\pi)^3 2E_l} \frac{2g_1^2}{s + m_\pi^2 - 2\sqrt{s}E_l - m_\rho^2 + i\epsilon}, \quad (4.7)$$

which demonstrates that, indeed,  $\tilde{G}_{\text{lim}}^{\text{FV}}$  can be obtained from  $\tilde{G}_{\text{lim}}^{\text{IV}}$  by the canonical substitution  $\int d^3l/(2\pi)^3 \rightarrow \sum_k l^3$ . In fact, we could have started from Eq. (4.7) all along and derived the quantization condition (4.6) from there, which shows that this quantization condition is semi-quantitative up to the discussed approximations.

Numerical results are shown in Fig. 8. As the left picture illustrates, the value of the lattice propagator  $\tilde{G}_{\text{lim}}^{\text{FV}}$  taken at  $\sqrt{s} = E_0$  (thin vertical line), slightly above threshold (dashed vertical line) determines  $\tilde{C}$  according to Eq. (4.6). The resulting values indeed exhibit a pole, as a function of the cutoff, as the picture to the right shows. It is remarkable how much this figure resembles the actual behavior of the singularity in  $\tilde{C}$  shown in Fig. 7.

In summary, the contact term  $\tilde{C}$  can exhibit singularities in the right kinematic conditions. This is a consequence of the current situation that  $\Delta E = E_0 - (m_\pi + m_\rho) > 0$  (overall repulsive three-body amplitude) and that  $b$  in Eq. (4.4) is a monotonous function of cutoff  $\Lambda$ , large enough to cancel  $a/\Delta E$ . The situation appears similar to the infinities in the contact term discussed in Ref. [47], but it is not identical. Here, we have a repulsive level and we do not observe bound states even for negative  $\tilde{C}$ , while in Ref. [47] the cyclic behavior of the contact term with  $\Lambda$ , for a pre-existing three-body bound state was investigated. For a recent study of similar structures in charm three-body systems see Ref. [123].

### C. Comparison with an effective Lagrangian

The three-body force (contact term  $\tilde{C}$ ) depends on the details of regularization [35, 124],  $\tilde{C} = \tilde{C}(\Lambda)$ . Still, one can match its size order-by-order to a given theory. For example, at leading order we may compare it to the predictions provided by the effective Lagrangian for the interaction between the octets of pseudoscalar and vector mesons, see Ref. [100]. This Lagrangian was used in Refs. [101, 102] as the kernel driving the unitarized interaction of these

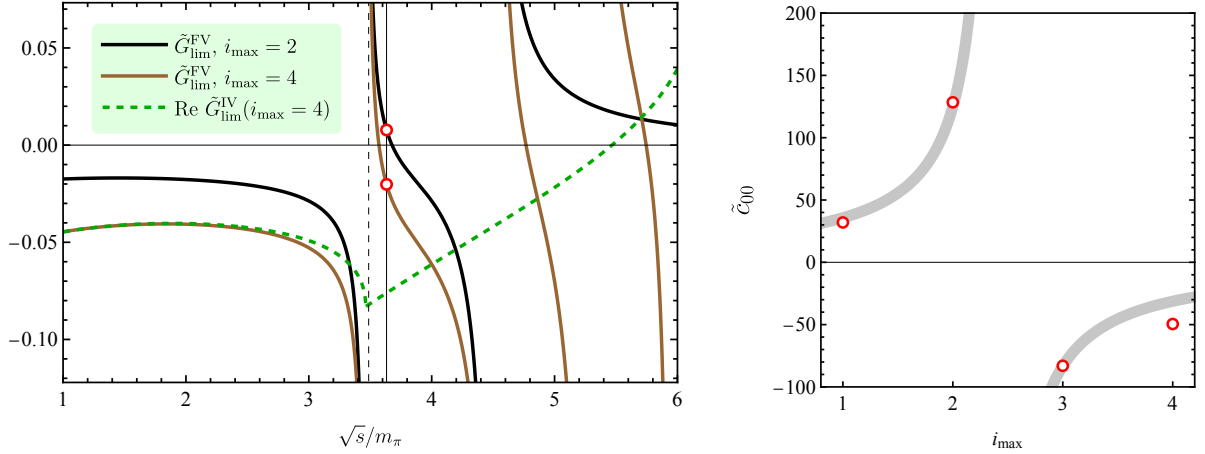


Figure 8. Left: Black and brown solid lines: Lattice propagator  $\tilde{G}_{\text{lim}}^{\text{FV}}$ , assuming a stable  $\rho$  and a stable  $\pi$  for different cutoffs (shell 2 and shell 4). For comparison, the real part of the infinite-volume propagator  $\tilde{G}_{\text{lim}}^{\text{IV}}$  is also shown (green dashed). The vertical line shows the choice of the measured energy level  $E_0$ , situated slightly above the  $\pi\rho$  threshold (compare also to Fig. 6). The red dots show two values of  $\tilde{C}_{00}^{-1}$  with different sign (cf. Eq. (4.6)) implying the possibility of a singularity,  $C_{00} = \infty$ . Right: The resulting  $\tilde{C}$ -term exhibits a singularity that explains the phenomenon observed for the full amplitude in Fig. 7. The gray line is to guide the eye.

mesons leading to the dynamical generation of several axial resonances, among them the  $a_1(1260)$ . Here, we need the isospin  $I = 2$  interaction of  $\pi\rho$  in  $S$ -wave to compare to the extracted  $\tilde{C}$ -term, that is,  $I^G(J^{PC}) = 2^-(1^{+-})$ .

The Lagrangian has been expanded to two pseudoscalar meson ( $P$ ) and two vector-mesons ( $V$ ) fields in Ref. [102] resulting for the relevant interacting part in

$$\mathcal{L} = -\frac{1}{4f_\pi^2} \langle [V^\mu, \partial^\nu V_\mu][P, \partial_\nu P] \rangle, \quad (4.8)$$

where the trace is taken over the octet matrices [102]. We evaluated the  $I = 2$  interaction and reproduced the results for other quantum numbers quoted in Ref. [102]. Assigning four-momenta and helicities as  $V(q, \lambda)P(p) \rightarrow V(q', \lambda')P(p')$ , the Feynman vertex is

$$C_{\lambda'\lambda}^{\text{eff}, I=2}(\mathbf{p}', \mathbf{p}) = -\epsilon_{\lambda\nu}(\mathbf{q})\epsilon_{\lambda'}^\nu(\mathbf{q}')^* \frac{(p+p')_\mu(q+q')^\mu}{2f_\pi^2}, \quad (4.9)$$

which happens to fulfill  $C^{\text{eff}, I=2} = -C^{\text{eff}, I=1}$ . Explicit expressions for the polarization vectors are given in the Appendix of Ref. [88]. Subsequently, this expression is partial-wave projected according to the Eq. (2.7) and transformed from helicity basis to  $JLS$ -basis using Eq. (2.10). Calling the resulting  $S$ -wave amplitude  $C_{00}^{\text{eff}}(\mathbf{p}', \mathbf{p})$ , where now  $\mathbf{p} = |\mathbf{p}|$ , the result is shown in Fig. 9 to the left with the solid red curve, transformed as

$$\tilde{C}_{00}^{\text{eff}}(\mathbf{p}', \mathbf{p}) = \frac{C_{00}^{\text{eff}}(\mathbf{p}', \mathbf{p})}{2g_1^2}. \quad (4.10)$$

The factor of 1/2 arises from a re-definition of the amplitude as explained following Eq. (2.6). The factor  $g_1^2$  comes from the observation that the term  $\tilde{B}$  of Eq. (2.3) is not at the level of a Feynman rule as factors  $g_1^2$  are missing. To match the Feynman rule of Eq. (4.8) one, therefore, has to divide it by  $g_1^2$ . Note also the compensating factor  $2g_1^2$  in Eq. (4.5). For the numerical comparison, we use  $f_\pi = 0.336$   $m_\pi$ ,  $m_\rho = 2.463$   $m_\pi$  at the heavy pion mass of  $m_\pi \approx 315$  MeV determined on the same ensemble [109], and  $g_1 = 5.8$  as before.

In the same plot, we show limits allowed by the lattice, i.e., the values of the  $\tilde{C}$  determined from a fit of method 1 of Eq. (2.23) to the ground level  $E_0 = 3.569(32)$   $m_\pi$ , using a momentum-independent  $\tilde{C}_{00}$  term. At the given cutoff ( $\Lambda_2, \Lambda_3, \Lambda_4$ ) for  $i_{\text{max}} = 2, 3, 4$  as explained following Eq. (2.31), the limits on the shaded areas of allowed values of  $\tilde{C}$  are determined by matching  $\tilde{C}$  to the extension of the  $1\sigma$  error bar of the lattice data,  $\sqrt{s} = E_0 - \Delta E$  and

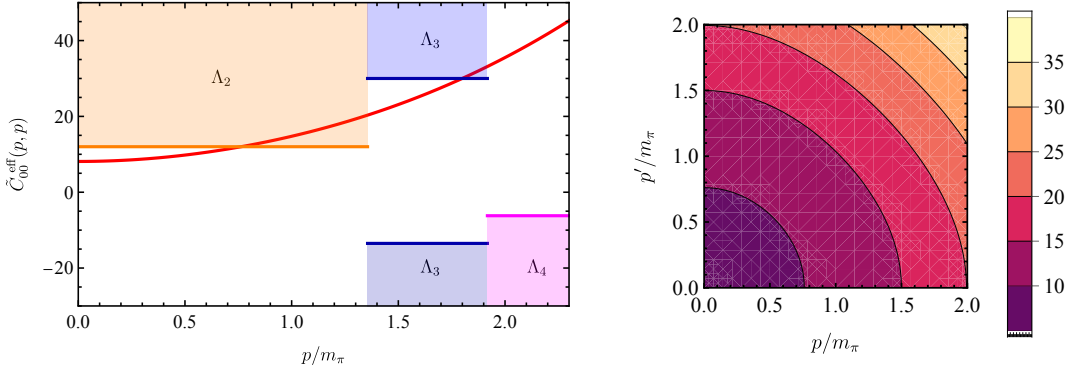


Figure 9. Left:  $S$ -wave projected  $\pi\rho$  interaction at the leading order from the effective Lagrangian of Ref. [100] (red solid line). The shaded areas show values for  $\tilde{C}_{00}^{\text{eff}}$  allowed to  $1\sigma$  by the ground state energy  $E_0$  from lattice QCD. These areas depend on the cutoff as indicated (shells 2-4 considered). The unusual cutoff dependence is discussed in the text. Right: Dependence of  $\tilde{C}_{00}^{\text{eff}}(p', p)$  on incoming and outgoing spectator momenta.

$\sqrt{s} = E_0 + \Delta E$ , see Fig. 6. Due to the singular behavior discussed in the previous subsection, allowed values can include  $\tilde{C}_{00} = \pm\infty$ . As the figure shows, the prediction from the effective Lagrangian lies at the borders of the  $1\sigma$  allowed region if the cutoff is not chosen too large. The effective Lagrangian predicts a repulsion of the  $\pi\rho$  interaction in the  $I = 2$  channel that is slightly smaller than the LQCD value.

## V. INFINITE-VOLUME AMPLITUDE

### A. Three-body amplitude

The infinite-volume amplitudes are obtained by solving Eq. (2.11) using the input obtained from fits to the finite-volume lattice QCD spectrum. That input consists of contact terms parameterizing the channel transitions listed in Tab. II and in the two-body phase-shifts entering through Eq. (2.21). We proceed here with results from fits 2, 6, and 7 (heavy pion mass and larger cutoff,  $i_{\text{max}} = 4$ ). The cutoff dependence is further discussed in Sect. V B.

The infinite-volume scattering equation (2.11) is solved along a complex contour as discussed in detail in Refs. [88, 94, 95]. In particular, there is a spectator momentum contour (SMC in  $l$  in Eq. (2.2)) and a self-energy contour (SEC in  $k$  in Eq. (2.21)). The former is chosen to avoid the three-body singularities in the  $\check{B}$  term from Eq. (2.36) and all singularities/branch points from the two-body amplitude, and the latter is chosen to avoid the usual two-body singularity for the calculation of  $\Sigma$  of Eq. (2.21) and the SMC. The SMC adopted here differs from that introduced in the three-body formalisms in Ref. [88] used later in different variations in Refs. [17, 19, 21, 94, 95]. Typically, such a contour starts at the origin, bends into the lower half of the complex momentum plane, and ends at the cutoff. In the present finite-volume formulation, however, a matching point at the two-body threshold  $\sigma_0 = 4m_\pi^2$  is introduced in Eq. (2.28). Contour deformation across this non-analyticity is forbidden so that the SMC must return to the real axis at the matching point before continuing along the real axis towards the cutoff. An example of such a contour in the complex  $\sigma$  plane is shown in Fig. 10. The location of the matching point in spectator momentum depends on the total three-body energy  $\sqrt{s}$ .

The infinite-volume amplitude is obtained for  $N = 60$  integration nodes of incoming and outgoing spectator momenta. The resulting matrix is of dimension  $3N$  corresponding to the three isospin/angular momentum channels in the  $JLS$  basis. To represent the amplitude we chose to calculate the production process that includes the rescattering amplitude  $\tilde{\Gamma}$  as a function of total energy and outgoing momentum according to Ref. [94]. This process starts with an elementary isobar-spectator production  $D$ , followed by the isobar-spectator propagation and undergoing three-body

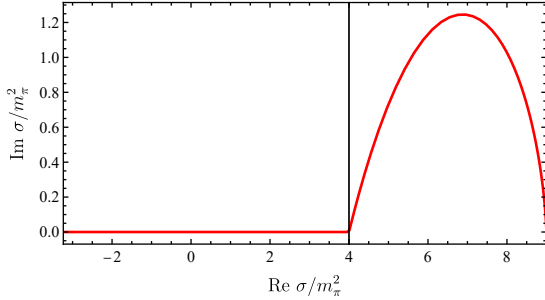
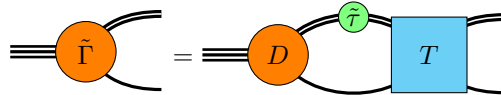


Figure 10. An example of the SMC mapped to the isobar sub-energy  $\sigma$  plane at  $\sqrt{s} = 4m_\pi$  with  $i_{\max} = 4$ . The contour consists of two segments: a complex segment in the upper-half plane and a real-axis segment beyond the matching point as required by analyticity. The vertical black line indicates the matching condition at  $\text{Re } \sigma_0 = 4m_\pi^2$ .

interaction,  $T$ :



$$\tilde{\Gamma}_j(s, q) = \int_{\Gamma} \frac{dp p^2}{(2\pi)^3 2E_p} T_{jk}(s, q, p) \tilde{\tau}_k(\sigma_p) D_k(s, p) , \quad (5.1)$$

where  $j, k$  are channel indices. In contrast to  $T(s, q, p)$  this quantity depends only on one momentum which makes it easier to examine numerical results. Note that three-body Dalitz plots with resonant channels can be calculated as demonstrated in Ref. [106] (FVU formalism) and more recently in Ref. [93] (RFT formalism). The relation of  $\tilde{\Gamma}$  to the physical  $1 \rightarrow 3$  production process is discussed below. In Eq. (5.1),  $D_k(s, p)$  is a real-valued, energy- and momentum-dependent production function, analogous to that employed in isobar analyses. We define it as

$$D_k(s, p) = D_{fk}(s, p) b_{L(k)}(\lambda p) , \quad (5.2)$$

where  $L(k)$  denotes the orbital angular momentum corresponding to channel  $k$ . Here,  $D_{fk}$  can additionally depend on spectator momentum and energy. The centrifugal barrier factors  $b_L$  scale with  $p^{L(k)}$  at low momenta, but then smoothly approach unity at higher momenta. This momentum suppression is regulated by the parameter  $\lambda$  [125]. For this paper, we chose  $\lambda = 0.5 m_\pi^{-1}$ ,  $D_{f0} = D_{f2} = m_\pi$  for the  $\pi\rho$  channels, and  $D_{f1} = 1$  for the  $\pi G$  channel. We also note that  $\tilde{\Gamma}$  still needs to be continued to real spectator momenta  $q$  for which we use a continued-fraction extrapolation method [95, 126]. These references provide also a comparison of different methods of analytic continuation in momentum.

Figure 11 shows the real (solid lines) and imaginary parts (dashed lines) of the rescattering term  $\tilde{\Gamma}$  of all three channels in terms of outgoing momentum  $q$ . The plot ends at the momentum corresponding to the isobar two-body thresholds, showing only the physical region. Firstly, we note that two of the fits (2 and 6) are almost indistinguishable in the  $(\pi\rho)_S$  and  $(\pi G)_P$  channels and very close in  $(\pi\rho)_D$  channel. For fit 2 we calculate the (correlated) statistical uncertainties through a resampling procedure with the result shown as the green bands.

The statistical uncertainties are substantially smaller than the spread between results when using different fit forms, i.e., using different parameterizations of the three-body force  $\tilde{C}$ . In particular, results change substantially for fit 7 (blue lines). Indeed, that fit exhibits a smaller  $\check{c}_{00}$  and larger  $\check{c}_{11}$  than the others as quoted in Tab. II. In other words, the  $\pi G$  interaction in that particular fit plays a larger role. More precise data could help in the determination of relative strengths of different channels. Still, there is a clear indication for sign and size of the  $S$ -wave and at least the sign for the  $D$ -wave seems to be determined. The result also shows the importance of using various parameterizations to avoid bias in the extracted physical picture.

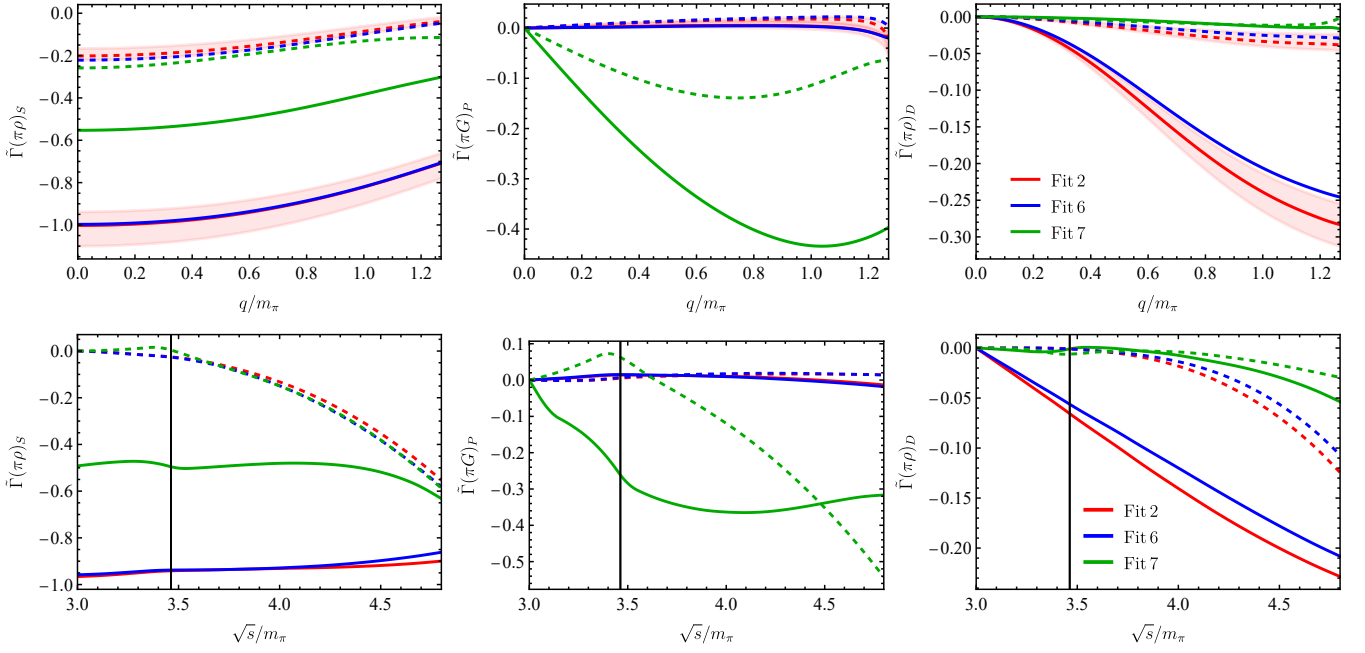


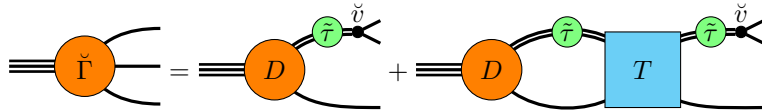
Figure 11. Top panel: The production amplitude [real(solid lines) and imaginary(dashed lines) parts]  $\tilde{\Gamma}_L(\sqrt{s} = 4m_\pi, q)$  of the fits to the heavy pion mass case with  $i_{max} = 4$ , i.e., fits 2, 6, 7 from Tab. II. Bottom panel:  $\tilde{\Gamma}(s, q = q_{max}/2)$  from Eq. (5.1). The black line indicates the pseudo-threshold,  $\sqrt{s} = m_\pi + m_\rho$  defined through  $\cot \delta^{11}(m_\rho) = 0$ , see Fig. 6. The bands in the upper plot show the statistical uncertainties for fit 2. For simplicity these bands are omitted in subsequent plots and for the other fits 6 and 7, and only best fit values are shown for them.

The bottom panel of Fig. 11 shows the energy dependence of the amplitude for a fixed  $q = q_{max}/2$ , i.e., half of the largest physical spectator momentum [88], see also Fig. 1,

$$q_{max}^2 = \frac{s^2 + 9m_\pi^4 - 10s m_\pi^2}{4s}. \quad (5.3)$$

For simplicity, we only show the central value of fit 2 (green lines) in the lower panel of Fig. 11 and subsequent figures. The most prominent feature is a kink in  $\tilde{\Gamma}$  of the  $(\pi\rho)_S$  outgoing state at around the lowest non-interacting  $\pi\rho$  level at  $\sqrt{s} = 3.46 m_\pi$  (see also Fig. 6). This structure is the  $\pi\rho$   $S$ -wave threshold cusp that appears “washed out” due to the finite  $\rho$  width. It is also visible for the  $\pi G$  final state through coupled-channel effects.

The full, physical  $1 \rightarrow 3$  production amplitude  $\tilde{\Gamma}$  contains not only the rescattering piece,  $\tilde{\Gamma}$ , but also a final isobar and its decay, as well as a disconnected piece as formulated in Ref. [94]. It reads



$$\tilde{\Gamma}_j(s, q') = N_j \tilde{v}_j(\sigma(q')) \tilde{\tau}_j(\sigma(q')) \left[ D_j(s, q') + \tilde{\Gamma}_j(s, q') \right]. \quad (5.4)$$

The  $\tilde{v}$  is the final decay vertex attached to the isobar. For the  $S$ -wave isobar decay,  $G \rightarrow \pi\pi$ , it is simply  $\tilde{v}_i = 1$  because  $\tilde{\tau}$  corresponds already to the full amplitude in plane-wave basis. For the  $P$ -wave isobar decay,  $\rho \rightarrow \pi\pi$ ,  $\tilde{v} \sim q_\sigma$  with  $q_\sigma$  the pion momentum defined in the  $\rho$  rest frame, see Ref. [94] for explicit expressions.

The lineshapes for fixed energy and momentum are shown in Fig. 12. To provide more quantitative insight into the effects of three-body rescattering we allow for a normalization  $N_j$  that is chosen such that the areas under all lineshapes are the same. For comparison, we also show the “disconnected part” with black dashed lines,  $N_j \tilde{v}_j \tilde{\tau}_j D_j$ . This part

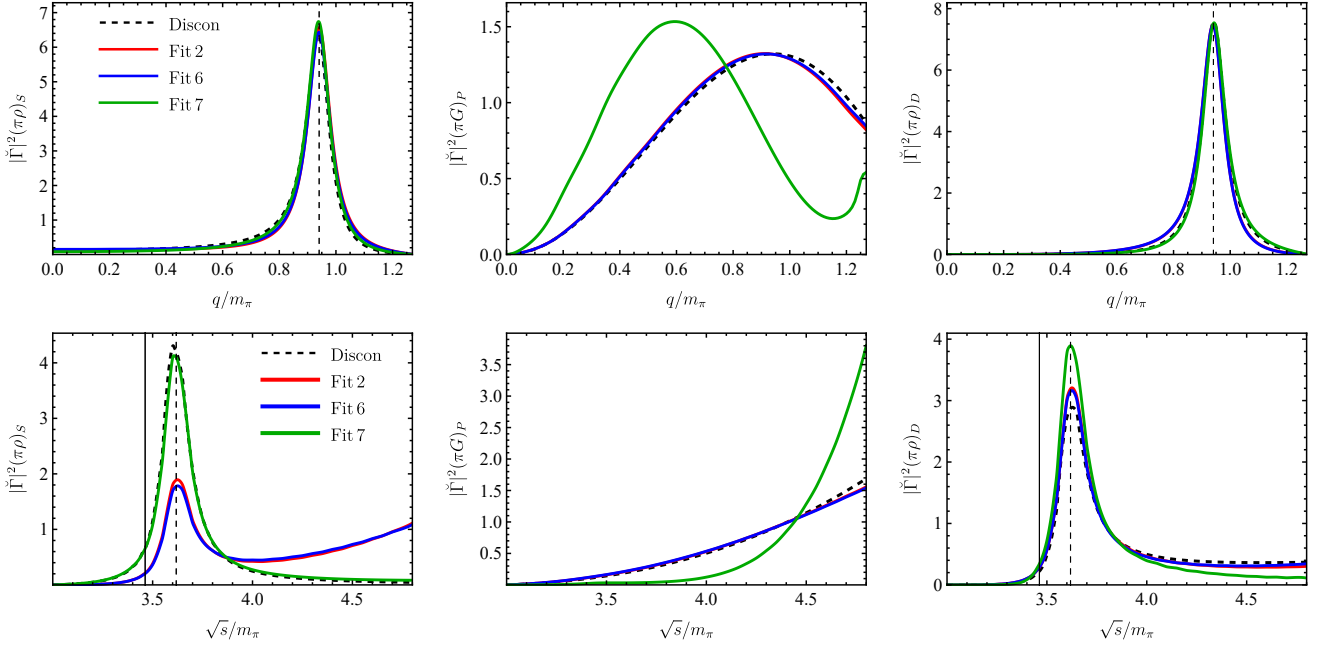


Figure 12. The normalized physical  $1 \rightarrow 3$  production amplitude  $\check{\Gamma}_L$ , ( $L = 0, 1, 2$ ) for fixed  $\sqrt{s} = 4m_\pi$  in terms of spectator momentum (upper panel), and for fixed  $q = q_{\max}/2$  in terms of three-body energy (lower panel), for fits 2, 6, 7 shown in red, blue, and green, respectively. The black dashed curves show the “disconnected” amplitude, corresponding to a lineshape without three-body interaction. The solid black vertical lines indicate the nominal  $\rho + \pi$  threshold, whereas the dashed vertical lines indicate the position of the  $\rho$  isobar.

contains no three-body rescattering and corresponds to the amplitude in a traditional isobar model. See Fig. 1 in Ref. [94] for a graphical representation. In such a model, the three-body dynamics is encoded in a complex-valued production mechanism (the “partial wave”) followed by a chain of isobar decays, while here we have a real-valued production mechanism  $D$ , followed by the explicit, complex-valued, and unitary three-body dynamics. Deviations of the lineshapes of fits 2, 6, and 7 from the disconnected part can, therefore, be attributed to the nontrivial three-body rescattering and coupled-channel effects calculated from lattice QCD.

The  $\rho$  lineshapes from the final isobar in Eq. (5.4) are clearly visible for both  $\pi\rho$  channels. In the upper panel of Fig. 12, the  $\rho$  peak appears at  $q(s) = q_{\text{cm}} := (\lambda(s, m_\pi^2, m_\rho^2))/(2\sqrt{s})$  (vertical dashed lines). In the lower panel, the  $\rho$  peak is shifted to the right of the nominal  $\pi\rho$  “threshold” (solid vertical lines) due to the chosen nonzero  $q = q_{\max}/2$  spectator momentum. In particular, the isobar position in  $\sqrt{s}$  is given by  $\sigma(s, q_{\max}(s)/2) = m_\rho^2$ .

Overall, the modifications to the lineshape appear moderate and of similar size as in Ref. [94] when plotted as a function of spectator momentum  $q$  (upper panel in Fig. 12), except in the  $\pi G$  channel for fit 7 that exhibits stronger  $\pi G$  rescattering than the other fits. If shown as a function of three-body energy (lower panel of Fig. 12), there can be noticeable differences at higher  $\sqrt{s}$ , even for the  $\pi\rho$  channels. Indeed, for fits 2 and 6, the lineshape reaches a comparable size as the isobar peak itself. This simply reflects the non-trivial energy dependence of the three-body amplitude which differs among the fits.

## B. Narrow $\rho$ -limit

To obtain additional insights into the dynamics of the system and the different fits, we take the limit of a narrow  $\rho$  meson. As mentioned before, the  $\rho$ -meson has a small width of  $\Gamma = 0.13m_\pi$  [109] at the heavier pion mass ensemble. At the same time, the  $\pi\rho$   $S$ -wave channel largely dominates the  $I = 2$  system close to threshold as Fig. 6 demonstrates. To illustrate the strength of the dominant  $\pi\rho$  channel, one can calculate the two-body “phase-shift” in the narrow- $\rho$

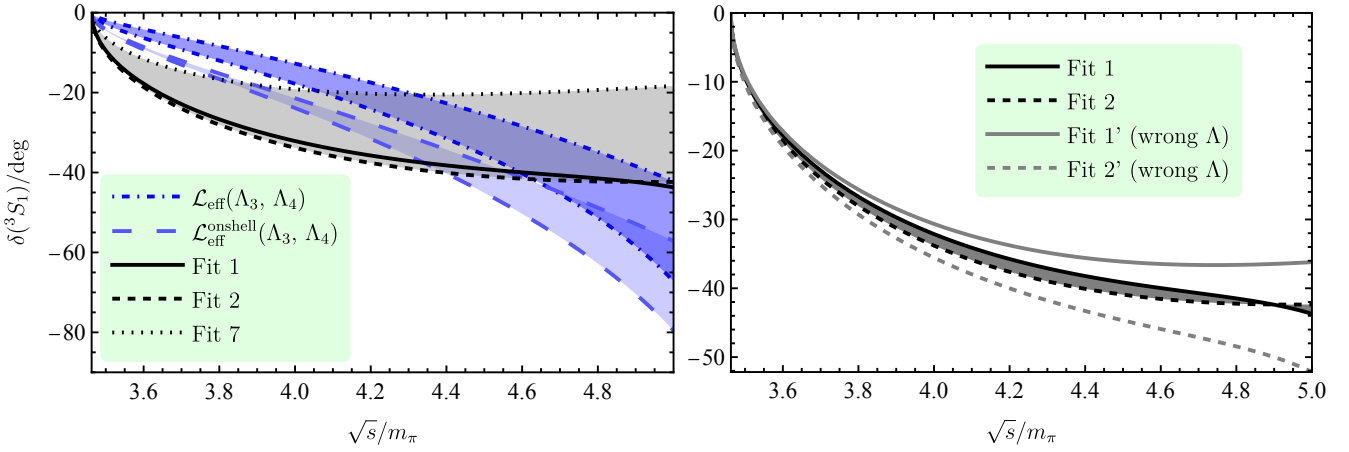


Figure 13. Left:  $\pi\rho$  S-wave “phase shifts” for the  $m_\pi = 315$  MeV ensemble assuming a stable  $\rho$ -meson and omitting the  $(\pi\rho)_D$  and  $\pi G$  channels. The black curves show results obtained from the central values of some fits to the LQCD data (fits 1, 2, and 7 according to Tab. II). The blue dashed lines show the predictions from the effective Lagrangian of Eq. (4.8) and their inherent cut-off dependence by using different cut-offs  $\Lambda_3$  and  $\Lambda_4$ .

Right: Fits 1 and 2 produce similar results demonstrating that cut-off dependence is effectively absorbed in fit parameter values. Indeed, evaluating the fits with exchanged cut-offs  $\Lambda_3 \leftrightarrow \Lambda_4$  (without refit) produces fits 1' and 2' that produce substantially different outcomes.

approximation. Obviously, this should not be mistaken for a representation of the full three-body dynamics discussed in the previous section. For this exercise we use the propagator from Eq. (4.7) and the fitted  $\check{C}_{00}$  for the  $\pi\rho$  channel, neglecting the sub-dominant  $\tilde{B}$  term and all channels other than  $(\pi\rho)_S$  for simplicity. Phase shifts are then calculated from the two-body unitary  $\bar{T}_{00}$  obtained by solving the following equation which is of Lippmann-Schwinger type with relativistic kinematics,

$$\bar{T}_{00}(s, p', p) = \bar{C}_{00}(s, p', p) + \int_0^\Lambda \frac{dl}{(2\pi)^3 2E_l} \frac{\bar{C}_{00}(s, p', l) 2g_1^2 \bar{T}_{00}(s, l, p)}{s + m_\pi^2 - 2\sqrt{s}E_l - m_\rho^2 + i\epsilon}, \quad \bar{C}_{00} \in \{\tilde{C}_{00}^{\text{eff}}, \check{C}_{00}\}, \quad (5.5)$$

which iterates either  $\tilde{C}_{00}^{\text{eff}}$  from Eq. (4.10) or the fitted  $\check{C}_{00}$  from Eq. (2.37).

The resulting phases are shown in Fig. 13 to the left for the representative fits 1, 2, and 7 according to Table II. We do not show fit 6 which would appear very similar to fit 2. Fitting all four lattice energies clearly restricts the phase-shift to be negative/repulsive in the entire energy window, in agreement to the situation at threshold, see discussion of of Fig. 6. The smallest phase-shift, clearly separated from the other black lines, originates from fit 7 (see Tab. II) in which the coupling to the  $\pi G$  channel plays an important role (fit 4 is very similar to 7 and not shown either). This emphasizes again the need for more LQCD data to better resolve the individual three-body channels.

The phase-shifts predicted from the effective Lagrangian of Eq. (4.8) are shown with the blue dash-dotted lines. Of course, these predictions are cutoff dependent and, therefore, shown for the typical values  $\Lambda_3$  and  $\Lambda_4$  used in this study. In agreement with the situation discussed for Fig. 9, we observe that the predicted repulsion at the  $\pi\rho$  threshold is at the lower end of results allowed by the LQCD calculation. However, one can now also see that, at larger energies, the effective Lagrangian predicts the same or even larger repulsion than observed in LQCD. We also study the off-shell dependence of these predictions by solving Eq. (5.5) with an onshell factorized interaction,  $\tilde{C}_{00}^{\text{eff}}(p' = p_{\text{cm}}, p = p_{\text{cm}})$  where  $p_{\text{cm}}$  is the onshell three-momentum of the pion and stable  $\rho$  meson in the center of mass. This leads to a noticeable change of results as indicated with the blue long-dashed lines. Overall, it is rather surprising how well the LQCD results are predicted by the effective interaction at the rather large pion mass of  $m_\pi = 315$  MeV.

On the right-hand side of Fig. 13 the cutoff dependence is illustrated. The gray shading connects fits 1 and 2 ( $i_{\text{max}} = 3, 4$ ) and shows little variation of results. This demonstrates that changes in cutoff can quite effectively be absorbed in the fit parameters. One can demonstrate that this renormalization works well by evaluating fits 1 and

2 with each other's cutoff, without refit. This leads to the wrong “fits” 1' and 2' that exhibit substantially larger discrepancies for the observables. Still, the overall cutoff dependence is moderate. One reason lies in the weakness of the interactions, making loops less relevant for the dynamics than in stronger interacting systems, such as three-body resonances [16, 19, 21]. The second reason lies in the effective suppression of high-momentum contributions through the form factor for the contact terms in Eq. (2.37) (note also the subtraction procedure for  $\check{B}$  from Eq. (2.36) even though this term is neglected in the present exercise). The moderate cutoff dependence also ensures that potential residual finite-volume effects from the cutoff are further suppressed as shown in Fig. 2.

Overall, the  $S$ -wave “phase-shifts” exhibit the same moderate repulsion as in Ref. [103]. In that study, the  $\rho$ -meson is a bound state due to the large pion mass ( $m_\pi \approx 700$  MeV). It is remarkable how much the phases resemble each other given the large difference in pion mass.

## VI. CONCLUSIONS

In this work we studied the three-pion system with  $I = 2$  using lattice QCD and a unitary coupled-channel three-body framework in finite and infinite-volume, referred to as Finite Volume Unitarity (FVU) [32, 104]. We extended the quantization condition to include isobars up to  $P$ -wave, i.e. the coupled channels  $\pi\rho$  and  $\pi G$ , where  $G$  stands for the isospin-2  $S$ -wave  $\pi\pi$  system. We also formulated a subtraction scheme for the three-body interaction that conserves unitarity while reducing the sensitivity to the hard cutoff and possible finite-volume effects tied to it.

The finite-volume spectrum of the system was determined in a dedicated lattice QCD calculation using GWQCD ensembles with two unphysical pion masses  $m_\pi \approx 315$  MeV and  $m_\pi \approx 224$  MeV. Using the coupled-channel quantization condition, three-body contact terms were fitted to the finite-volume spectrum in the elastic window and mapped to the infinite-volume amplitudes, thus, predicting three-body rescattering contributions and  $1 \rightarrow 3$  three-pion production amplitudes. Exploring different parametrizations for the channel transitions revealed that the sign and size of the real part of the dominant  $(\pi\rho)_S$  amplitude can be determined within large (mostly systematic) uncertainties.

A qualitative study at threshold revealed that the dynamics is repulsive: one-pion exchange in the  $\pi\rho$  channel gives only a small attractive contribution, the  $\pi G$  channel provides an even smaller repulsion, and the observed net repulsion requires a repulsive short-range three-body interaction. In addition, we compared the extracted interaction pattern with the predictions from a leading-order effective  $\pi\rho$  Lagrangian and found a repulsion of comparable size although the prediction is, of course, regularization dependent.

To further interpret the dynamics, the limit of a narrow  $\rho$  was considered. In this limit, the system reduces to an effective two-body problem, allowing a definition of a  $\pi\rho$  “phase shift” for the dominant  $S$ -wave channel. The resulting “phases” from LQCD are negative with a typical size of  $-20^\circ$  to  $-40^\circ$ , which is consistent with the repulsive behavior inferred from the full coupled-channel analysis.

In conclusion, the present study is limited by the available lattice information, with only a few levels in a single irrep at unphysical pion masses, affecting the determination of the amplitudes and individual isobar channels. Yet, through the inclusion of constraints from effective field theories it was, indeed, possible to isolate the repulsive nature of the dominant  $(\pi\rho)_S$  channel in agreement with predictions of an effective Lagrangian. To reach more quantitative conclusions, future work should include additional volumes and boosts. A naive chiral extrapolation of the  $m_\pi = 315$  MeV lattice spectrum with FVU successfully predicts the lattice spectrum at  $m_\pi = 224$  MeV, but higher precision data at that and lighter pion masses would allow for a better determination of chiral trajectories of the  $\pi\rho$  interaction.

## ACKNOWLEDGMENTS

We are grateful to Michael Birse for discussions and also thank ECT\* for support at the Workshop “Universality in strongly-interacting systems: from QCD to atoms” during which corresponding discussions occurred. We also thank Hans-Werner Hammer, Yong-Hui Lin and Raquel Molina for useful discussions. The work of YF, MD, and MM was

supported by the National Science Foundation (NSF) Grant No. 2310036. The work of MM was further funded through the Heisenberg Programme by the Deutsche Forschungsgemeinschaft (DFG, German Research Foundation) – 532635001. The work of CC, FXL, and AA was supported by US Department of Energy grant DE-FG02-95ER40907. This material is based upon work supported by the U.S. Department of Energy, Office of Science, Office of Nuclear Physics under contract DE-AC05-06OR23177.

---

[1] Maxim Mai, Ulf-G. Meißner, and Carsten Urbach, “Towards a theory of hadron resonances,” *Phys. Rept.* **1001**, 1–66 (2023), [arXiv:2206.01477 \[hep-ph\]](https://arxiv.org/abs/2206.01477).

[2] Richard A. Arndt, Igor I. Strakovsky, Ron L. Workman, and Marcello M. Pavan, “Updated analysis of  $\pi$  N elastic scattering data to 2.1-GeV: The Baryon spectrum,” *Phys. Rev. C* **52**, 2120–2130 (1995), [arXiv:nucl-th/9505040](https://arxiv.org/abs/nucl-th/9505040).

[3] L. Alvarez-Ruso, “On the nature of the Roper resonance,” in *Mini-Workshop Bled 2010: Dressing Hadrons* (2010) pp. 1–8, [arXiv:1011.0609 \[nucl-th\]](https://arxiv.org/abs/1011.0609).

[4] D. Rönchen, M. Döring, F. Huang, H. Haberzettl, J. Haidenbauer, C. Hanhart, S. Krewald, U. G. Meißner, and K. Nakayama, “Coupled-channel dynamics in the reactions  $\pi$ N  $\rightarrow$   $\pi$ N,  $\eta$ N, K $\Lambda$ , K $\Sigma$ ,” *Eur. Phys. J. A* **49**, 44 (2013), [arXiv:1211.6998 \[nucl-th\]](https://arxiv.org/abs/1211.6998).

[5] C. B. Lang, L. Leskovec, M. Padmanath, and S. Prelovsek, “Pion-nucleon scattering in the Roper channel from lattice QCD,” *Phys. Rev. D* **95**, 014510 (2017), [arXiv:1610.01422 \[hep-lat\]](https://arxiv.org/abs/1610.01422).

[6] Adrian L. Kiratidis, Waseem Kamleh, Derek B. Leinweber, Zhan-Wei Liu, Finn M. Stokes, and Anthony W. Thomas, “Search for low-lying lattice QCD eigenstates in the Roper regime,” *Phys. Rev. D* **95**, 074507 (2017), [arXiv:1608.03051 \[hep-lat\]](https://arxiv.org/abs/1608.03051).

[7] Zhan-Wei Liu, Waseem Kamleh, Derek B. Leinweber, Finn M. Stokes, Anthony W. Thomas, and Jia-Jun Wu, “Hamiltonian effective field theory study of the  $N^*(1440)$  resonance in lattice QCD,” *Phys. Rev. D* **95**, 034034 (2017), [arXiv:1607.04536 \[nucl-th\]](https://arxiv.org/abs/1607.04536).

[8] Ben Hörz and Andrew Hanlon, “Two- and three-pion finite-volume spectra at maximal isospin from lattice QCD,” *Phys. Rev. Lett.* **123**, 142002 (2019), [arXiv:1905.04277 \[hep-lat\]](https://arxiv.org/abs/1905.04277).

[9] Chris Culver, Maxim Mai, Ruairí Brett, Andrei Alexandru, and Michael Döring, “Three pion spectrum in the  $I = 3$  channel from lattice QCD,” *Phys. Rev. D* **101**, 114507 (2020), [arXiv:1911.09047 \[hep-lat\]](https://arxiv.org/abs/1911.09047).

[10] Matthias Fischer, Bartosz Kostrzewa, Liuming Liu, Fernando Romero-López, Martin Ueding, and Carsten Urbach, “Scattering of two and three physical pions at maximal isospin from lattice QCD,” *Eur. Phys. J. C* **81**, 436 (2021), [arXiv:2008.03035 \[hep-lat\]](https://arxiv.org/abs/2008.03035).

[11] Maxwell T. Hansen, Raul A. Briceño, Robert G. Edwards, Christopher E. Thomas, and David J. Wilson (Hadron Spectrum), “Energy-Dependent  $\pi^+\pi^+\pi^+$  Scattering Amplitude from QCD,” *Phys. Rev. Lett.* **126**, 012001 (2021), [arXiv:2009.04931 \[hep-lat\]](https://arxiv.org/abs/2009.04931).

[12] Andrei Alexandru, Ruairí Brett, Chris Culver, Michael Döring, Dehua Guo, Frank X. Lee, and Maxim Mai, “Finite-volume energy spectrum of the  $K^-K^-K^-$  system,” *Phys. Rev. D* **102**, 114523 (2020), [arXiv:2009.12358 \[hep-lat\]](https://arxiv.org/abs/2009.12358).

[13] Tyler D. Blanton, Andrew D. Hanlon, Ben Hörz, Colin Morningstar, Fernando Romero-López, and Stephen R. Sharpe, “Interactions of two and three mesons including higher partial waves from lattice QCD,” *JHEP* **10**, 023 (2021), [arXiv:2106.05590 \[hep-lat\]](https://arxiv.org/abs/2106.05590).

[14] S. R. Beane *et al.* (NPLQCD, QCDSF), “Charged multihadron systems in lattice QCD+QED,” *Phys. Rev. D* **103**, 054504 (2021), [arXiv:2003.12130 \[hep-lat\]](https://arxiv.org/abs/2003.12130).

[15] Patrick Bühlmann and Urs Wenger, “Finite-volume effects and meson scattering in the 2-flavour Schwinger model,” *PoS LATTICE2021*, 463 (2022), [arXiv:2112.15228 \[hep-lat\]](https://arxiv.org/abs/2112.15228).

[16] Maxim Mai, Andrei Alexandru, Ruairí Brett, Chris Culver, Michael Döring, Frank X. Lee, and Daniel Sadasivan (GWQCD), “Three-Body Dynamics of the a1(1260) Resonance from Lattice QCD,” *Phys. Rev. Lett.* **127**, 222001 (2021), [arXiv:2107.03973 \[hep-lat\]](https://arxiv.org/abs/2107.03973).

[17] Marco Garofalo, Maxim Mai, Fernando Romero-López, Akaki Rusetsky, and Carsten Urbach, “Three-body resonances in the  $\varphi^4$  theory,” *JHEP* **02**, 252 (2023), [arXiv:2211.05605 \[hep-lat\]](https://arxiv.org/abs/2211.05605).

[18] Zachary T. Draper, Andrew D. Hanlon, Ben Hörz, Colin Morningstar, Fernando Romero-López, and Stephen R. Sharpe, “Interactions of  $\pi K$ ,  $\pi\pi K$  and  $KK\pi$  systems at maximal isospin from lattice QCD,” *JHEP* **05**, 137 (2023), [arXiv:2302.13587](https://arxiv.org/abs/2302.13587)

[hep-lat].

[19] Haobo Yan, Maxim Mai, Marco Garofalo, Ulf-G. Meißner, Chuan Liu, Liuming Liu, and Carsten Urbach, “ $\omega$  Meson from Lattice QCD,” *Phys. Rev. Lett.* **133**, 211906 (2024), [arXiv:2407.16659 \[hep-lat\]](#).

[20] Sebastian M. Dawid, Fernando Romero-López, and Stephen R. Sharpe, “Finite- and infinite-volume study of  $DD\pi$  scattering,” *JHEP* **01**, 060 (2025), [arXiv:2409.17059 \[hep-lat\]](#).

[21] Haobo Yan, Maxim Mai, Marco Garofalo, Yuchuan Feng, Michael Döring, Chuan Liu, Liuming Liu, Ulf-G. Meißner, and Carsten Urbach, “Emergence of the  $\pi(1300)$  Resonance from Lattice QCD,” (2025), [arXiv:2510.09476 \[hep-lat\]](#).

[22] Silas R. Beane, William Detmold, Thomas C. Luu, Kostas Orginos, Martin J. Savage, and Aaron Torok, “Multi-Pion Systems in Lattice QCD and the Three-Pion Interaction,” *Phys. Rev. Lett.* **100**, 082004 (2008), [arXiv:0710.1827 \[hep-lat\]](#).

[23] K. Polejaeva and A. Rusetsky, “Three particles in a finite volume,” *Eur. Phys. J. A* **48**, 67 (2012), [arXiv:1203.1241 \[hep-lat\]](#).

[24] Raul A. Briceño and Zohreh Davoudi, “Three-particle scattering amplitudes from a finite volume formalism,” *Phys. Rev. D* **87**, 094507 (2013), [arXiv:1212.3398 \[hep-lat\]](#).

[25] Ulf-G. Meißner, Guillermo Ríos, and Akaki Rusetsky, “Spectrum of three-body bound states in a finite volume,” *Phys. Rev. Lett.* **114**, 091602 (2015), [Erratum: *Phys. Rev. Lett.* 117, 069902 (2016)], [arXiv:1412.4969 \[hep-lat\]](#).

[26] Maxwell T. Hansen and Stephen R. Sharpe, “Relativistic, model-independent, three-particle quantization condition,” *Phys. Rev. D* **90**, 116003 (2014), [arXiv:1408.5933 \[hep-lat\]](#).

[27] M. Jansen, H. W. Hammer, and Yu Jia, “Finite volume corrections to the binding energy of the  $X(3872)$ ,” *Phys. Rev. D* **92**, 114031 (2015), [arXiv:1505.04099 \[hep-ph\]](#).

[28] Maxwell T. Hansen and Stephen R. Sharpe, “Expressing the three-particle finite-volume spectrum in terms of the three-to-three scattering amplitude,” *Phys. Rev. D* **92**, 114509 (2015), [arXiv:1504.04248 \[hep-lat\]](#).

[29] Maxwell T. Hansen and Stephen R. Sharpe, “Perturbative results for two and three particle threshold energies in finite volume,” *Phys. Rev. D* **93**, 014506 (2016), [arXiv:1509.07929 \[hep-lat\]](#).

[30] Maxwell T. Hansen and Stephen R. Sharpe, “Threshold expansion of the three-particle quantization condition,” *Phys. Rev. D* **93**, 096006 (2016), [Erratum: *Phys. Rev. D* 96, 039901 (2017)], [arXiv:1602.00324 \[hep-lat\]](#).

[31] Peng Guo, “One spatial dimensional finite volume three-body interaction for a short-range potential,” *Phys. Rev. D* **95**, 054508 (2017), [arXiv:1607.03184 \[hep-lat\]](#).

[32] M. Mai and M. Döring, “Three-body Unitarity in the Finite Volume,” *Eur. Phys. J. A* **53**, 240 (2017), [arXiv:1709.08222 \[hep-lat\]](#).

[33] Sebastian König and Dean Lee, “Volume Dependence of N-Body Bound States,” *Phys. Lett. B* **779**, 9–15 (2018), [arXiv:1701.00279 \[hep-lat\]](#).

[34] Hans-Werner Hammer, Jin-Yi Pang, and A. Rusetsky, “Three-particle quantization condition in a finite volume: 1. The role of the three-particle force,” *JHEP* **09**, 109 (2017), [arXiv:1706.07700 \[hep-lat\]](#).

[35] H. W. Hammer, J. Y. Pang, and A. Rusetsky, “Three particle quantization condition in a finite volume: 2. general formalism and the analysis of data,” *JHEP* **10**, 115 (2017), [arXiv:1707.02176 \[hep-lat\]](#).

[36] Raúl A. Briceño, Maxwell T. Hansen, and Stephen R. Sharpe, “Relating the finite-volume spectrum and the two- and three-particle  $S$  matrix for relativistic systems of identical scalar particles,” *Phys. Rev. D* **95**, 074510 (2017), [arXiv:1701.07465 \[hep-lat\]](#).

[37] Stephen R. Sharpe, “Testing the threshold expansion for three-particle energies at fourth order in  $\phi^4$  theory,” *Phys. Rev. D* **96**, 054515 (2017), [Erratum: *Phys. Rev. D* 98, 099901 (2018)], [arXiv:1707.04279 \[hep-lat\]](#).

[38] Peng Guo and Vladimir Gasparian, “Numerical approach for finite volume three-body interaction,” *Phys. Rev. D* **97**, 014504 (2018), [arXiv:1709.08255 \[hep-lat\]](#).

[39] Peng Guo and Vladimir Gasparian, “A solvable three-body model in finite volume,” *Phys. Lett. B* **774**, 441–445 (2017), [arXiv:1701.00438 \[hep-lat\]](#).

[40] Yu Meng, Chuan Liu, Ulf-G Meißner, and A. Rusetsky, “Three-particle bound states in a finite volume: unequal masses and higher partial waves,” *Phys. Rev. D* **98**, 014508 (2018), [arXiv:1712.08464 \[hep-lat\]](#).

[41] Peng Guo, Michael Döring, and Adam P. Szczepaniak, “Variational approach to  $N$ -body interactions in finite volume,” *Phys. Rev. D* **98**, 094502 (2018), [arXiv:1810.01261 \[hep-lat\]](#).

[42] Peng Guo and Tyler Morris, “Multiple-particle interaction in (1+1)-dimensional lattice model,” *Phys. Rev. D* **99**, 014501 (2019), [arXiv:1808.07397 \[hep-lat\]](#).

[43] P. Klos, S. König, H. W. Hammer, J. E. Lynn, and A. Schwenk, “Signatures of few-body resonances in finite volume,” *Phys. Rev. C* **98**, 034004 (2018), [arXiv:1805.02029 \[nucl-th\]](#).

[44] Raúl A. Briceño, Maxwell T. Hansen, and Stephen R. Sharpe, “Numerical study of the relativistic three-body quantization

condition in the isotropic approximation,” *Phys. Rev. D* **98**, 014506 (2018), [arXiv:1803.04169 \[hep-lat\]](https://arxiv.org/abs/1803.04169).

[45] Raúl A. Briceño, Maxwell T. Hansen, and Stephen R. Sharpe, “Three-particle systems with resonant subprocesses in a finite volume,” *Phys. Rev. D* **99**, 014516 (2019), [arXiv:1810.01429 \[hep-lat\]](https://arxiv.org/abs/1810.01429).

[46] Maxim Mai and Michael Döring, “Finite-Volume Spectrum of  $\pi^+\pi^+$  and  $\pi^+\pi^+\pi^+$  Systems,” *Phys. Rev. Lett.* **122**, 062503 (2019), [arXiv:1807.04746 \[hep-lat\]](https://arxiv.org/abs/1807.04746).

[47] M. Döring, H. W. Hammer, M. Mai, J. Y. Pang, § A. Rusetsky, and J. Wu, “Three-body spectrum in a finite volume: the role of cubic symmetry,” *Phys. Rev. D* **97**, 114508 (2018), [arXiv:1802.03362 \[hep-lat\]](https://arxiv.org/abs/1802.03362).

[48] A. W. Jackura, S. M. Dawid, C. Fernández-Ramírez, V. Mathieu, M. Mikhaseko, A. Pilloni, S. R. Sharpe, and A. P. Szczepaniak, “Equivalence of three-particle scattering formalisms,” *Phys. Rev. D* **100**, 034508 (2019), [arXiv:1905.12007 \[hep-ph\]](https://arxiv.org/abs/1905.12007).

[49] M. Mai, M. Döring, C. Culver, and A. Alexandru, “Three-body unitarity versus finite-volume  $\pi^+\pi^+\pi^+$  spectrum from lattice QCD,” *Phys. Rev. D* **101**, 054510 (2020), [arXiv:1909.05749 \[hep-lat\]](https://arxiv.org/abs/1909.05749).

[50] Peng Guo, “Propagation of particles on a torus,” *Phys. Lett. B* **804**, 135370 (2020), [arXiv:1908.08081 \[hep-lat\]](https://arxiv.org/abs/1908.08081).

[51] Tyler D. Blanton, Fernando Romero-López, and Stephen R. Sharpe, “Implementing the three-particle quantization condition including higher partial waves,” *JHEP* **03**, 106 (2019), [arXiv:1901.07095 \[hep-lat\]](https://arxiv.org/abs/1901.07095).

[52] Raúl A. Briceño, Maxwell T. Hansen, Stephen R. Sharpe, and Adam P. Szczepaniak, “Unitarity of the infinite-volume three-particle scattering amplitude arising from a finite-volume formalism,” *Phys. Rev. D* **100**, 054508 (2019), [arXiv:1905.11188 \[hep-lat\]](https://arxiv.org/abs/1905.11188).

[53] Fernando Romero-López, Stephen R. Sharpe, Tyler D. Blanton, Raúl A. Briceño, and Maxwell T. Hansen, “Numerical exploration of three relativistic particles in a finite volume including two-particle resonances and bound states,” *JHEP* **10**, 007 (2019), [arXiv:1908.02411 \[hep-lat\]](https://arxiv.org/abs/1908.02411).

[54] Jin-Yi Pang, Jia-Jun Wu, H. W. Hammer, Ulf-G. Meißner, and Akaki Rusetsky, “Energy shift of the three-particle system in a finite volume,” *Phys. Rev. D* **99**, 074513 (2019), [arXiv:1902.01111 \[hep-lat\]](https://arxiv.org/abs/1902.01111).

[55] Peng Guo and Michael Döring, “Lattice model of heavy-light three-body system,” *Phys. Rev. D* **101**, 034501 (2020), [arXiv:1910.08624 \[hep-lat\]](https://arxiv.org/abs/1910.08624).

[56] Shangguo Zhu and Shina Tan, “ $d$ -dimensional Lüscher’s formula and the near-threshold three-body states in a finite volume,” (2019), [arXiv:1905.05117 \[nucl-th\]](https://arxiv.org/abs/1905.05117).

[57] Jin-Yi Pang, Jia-Jun Wu, and Li-Sheng Geng, “DDK system in finite volume,” *Phys. Rev. D* **102**, 114515 (2020), [arXiv:2008.13014 \[hep-lat\]](https://arxiv.org/abs/2008.13014).

[58] Maxwell T. Hansen, Fernando Romero-López, and Stephen R. Sharpe, “Generalizing the relativistic quantization condition to include all three-pion isospin channels,” *JHEP* **07**, 047 (2020), [Erratum: *JHEP* 02, 014 (2021)], [arXiv:2003.10974 \[hep-lat\]](https://arxiv.org/abs/2003.10974).

[59] Peng Guo, “Modeling few-body resonances in finite volume,” *Phys. Rev. D* **102**, 054514 (2020), [arXiv:2007.12790 \[hep-lat\]](https://arxiv.org/abs/2007.12790).

[60] Peng Guo, “Threshold expansion formula of  $N$  bosons in a finite volume from a variational approach,” *Phys. Rev. D* **101**, 054512 (2020), [arXiv:2002.04111 \[hep-lat\]](https://arxiv.org/abs/2002.04111).

[61] Peng Guo and Bingwei Long, “Visualizing resonances in finite volume,” *Phys. Rev. D* **102**, 074508 (2020), [arXiv:2007.10895 \[hep-lat\]](https://arxiv.org/abs/2007.10895).

[62] Peng Guo and Bingwei Long, “Multi-  $\pi^+$  systems in a finite volume,” *Phys. Rev. D* **101**, 094510 (2020), [arXiv:2002.09266 \[hep-lat\]](https://arxiv.org/abs/2002.09266).

[63] Tyler D. Blanton and Stephen R. Sharpe, “Alternative derivation of the relativistic three-particle quantization condition,” *Phys. Rev. D* **102**, 054520 (2020), [arXiv:2007.16188 \[hep-lat\]](https://arxiv.org/abs/2007.16188).

[64] Tyler D. Blanton and Stephen R. Sharpe, “Relativistic three-particle quantization condition for nondegenerate scalars,” *Phys. Rev. D* **103**, 054503 (2021), [arXiv:2011.05520 \[hep-lat\]](https://arxiv.org/abs/2011.05520).

[65] Fabian Müller, Tiansu Yu, and Akaki Rusetsky, “Finite-volume energy shift of the three-pion ground state,” *Phys. Rev. D* **103**, 054506 (2021), [arXiv:2011.14178 \[hep-lat\]](https://arxiv.org/abs/2011.14178).

[66] Fabian Müller and Akaki Rusetsky, “On the three-particle analog of the Lellouch-Lüscher formula,” *JHEP* **03**, 152 (2021), [arXiv:2012.13957 \[hep-lat\]](https://arxiv.org/abs/2012.13957).

[67] Andrew W. Jackura, Raúl A. Briceño, Sebastian M. Dawid, Md Habib E. Islam, and Connor McCarty, “Solving relativistic three-body integral equations in the presence of bound states,” *Phys. Rev. D* **104**, 014507 (2021), [arXiv:2010.09820 \[hep-lat\]](https://arxiv.org/abs/2010.09820).

[68] Ruairí Brett, Chris Culver, Maxim Mai, Andrei Alexandru, Michael Döring, and Frank X. Lee, “Three-body interactions from the finite-volume QCD spectrum,” *Phys. Rev. D* **104**, 014501 (2021), [arXiv:2101.06144 \[hep-lat\]](https://arxiv.org/abs/2101.06144).

[69] Fabian Müller, Jin-Yi Pang, Akaki Rusetsky, and Jia-Jun Wu, “Relativistic-invariant formulation of the NREFT three-

particle quantization condition,” *JHEP* **02**, 158 (2022), [arXiv:2110.09351 \[hep-lat\]](#).

[70] Maxwell T. Hansen, Fernando Romero-López, and Stephen R. Sharpe, “Decay amplitudes to three hadrons from finite-volume matrix elements,” *JHEP* **04**, 113 (2021), [arXiv:2101.10246 \[hep-lat\]](#).

[71] Tyler D. Blanton and Stephen R. Sharpe, “Three-particle finite-volume formalism for  $\pi+\pi+K+$  and related systems,” *Phys. Rev. D* **104**, 034509 (2021), [arXiv:2105.12094 \[hep-lat\]](#).

[72] Tyler D. Blanton, Fernando Romero-López, and Stephen R. Sharpe, “Implementing the three-particle quantization condition for  $\pi^+\pi^+K^+$  and related systems,” *JHEP* **02**, 098 (2022), [arXiv:2111.12734 \[hep-lat\]](#).

[73] Fabian Müller, Jin-Yi Pang, Akaki Rusetsky, and Jia-Jun Wu, “Three-particle Lellouch-Lüscher formalism in moving frames,” *JHEP* **02**, 214 (2023), [arXiv:2211.10126 \[hep-lat\]](#).

[74] Jin-Yi Pang, Martin Ebert, Hans-Werner Hammer, Fabian Müller, Akaki Rusetsky, and Jia-Jun Wu, “Spurious poles in a finite volume,” *JHEP* **07**, 019 (2022), [arXiv:2204.04807 \[hep-lat\]](#).

[75] Andrew W. Jackura and Raúl A. Briceño, “Partial-wave projection of the one-particle exchange in three-body scattering amplitudes,” (2023), [arXiv:2312.00625 \[hep-ph\]](#).

[76] Jin-Yi Pang, Rishabh Bubna, Fabian Müller, Akaki Rusetsky, and Jia-Jun Wu, “Lellouch-Lüscher factor for the  $K \rightarrow 3\pi$  decays,” (2023), [arXiv:2312.04391 \[hep-lat\]](#).

[77] Rishabh Bubna, Fabian Müller, and Akaki Rusetsky, “Finite-volume energy shift of the three-nucleon ground state,” *Phys. Rev. D* **108**, 014518 (2023), [arXiv:2304.13635 \[hep-lat\]](#).

[78] Zachary T. Draper, Maxwell T. Hansen, Fernando Romero-López, and Stephen R. Sharpe, “Three relativistic neutrons in a finite volume,” *JHEP* **07**, 226 (2023), [arXiv:2303.10219 \[hep-lat\]](#).

[79] Maxwell T. Hansen, Fernando Romero-López, and Stephen R. Sharpe, “Finite-volume formalism for  $N\pi\pi$  at maximal isospin,” (2025), [arXiv:2509.24778 \[hep-lat\]](#).

[80] Wilder Schaaf and Stephen R. Sharpe, “Implementing the three-neutron quantization condition,” (2025), [arXiv:2512.24508 \[hep-lat\]](#).

[81] Andrew W. Jackura, “Three-body scattering and quantization conditions from S-matrix unitarity,” *Phys. Rev. D* **108**, 034505 (2023), [arXiv:2208.10587 \[hep-lat\]](#).

[82] Tyler D. Blanton and Stephen R. Sharpe, “Equivalence of relativistic three-particle quantization conditions,” *Phys. Rev. D* **102**, 054515 (2020), [arXiv:2007.16190 \[hep-lat\]](#).

[83] Maxwell T. Hansen and Stephen R. Sharpe, “Lattice QCD and Three-particle Decays of Resonances,” *Ann. Rev. Nucl. Part. Sci.* **69**, 65–107 (2019), [arXiv:1901.00483 \[hep-lat\]](#).

[84] Maxim Mai, Michael Döring, and Akaki Rusetsky, “Multi-particle systems on the lattice and chiral extrapolations: a brief review,” *Eur. Phys. J. ST* **230**, 1623–1643 (2021), [arXiv:2103.00577 \[hep-lat\]](#).

[85] Stephen R. Sharpe, “Three-particle scattering amplitudes from lattice QCD,” in *42th International Symposium on Lattice Field Theory* (2026) [arXiv:2601.04147 \[hep-lat\]](#).

[86] M. Döring, C. Hanhart, F. Huang, S. Krewald, and U. G. Meißner, “Analytic properties of the scattering amplitude and resonances parameters in a meson exchange model,” *Nucl. Phys. A* **829**, 170–209 (2009), [arXiv:0903.4337 \[nucl-th\]](#).

[87] N. Suzuki, B. Julia-Diaz, H. Kamano, T. S. H. Lee, A. Matsuyama, and T. Sato, “Disentangling the Dynamical Origin of P-11 Nucleon Resonances,” *Phys. Rev. Lett.* **104**, 042302 (2010), [arXiv:0909.1356 \[nucl-th\]](#).

[88] Daniel Sadasivan, Andrei Alexandru, Hakan Akdag, Felipe Amorim, Ruairí Brett, Chris Culver, Michael Döring, Frank X. Lee, and Maxim Mai, “Pole position of the a1(1260) resonance in a three-body unitary framework,” *Phys. Rev. D* **105**, 054020 (2022), [arXiv:2112.03355 \[hep-ph\]](#).

[89] Sebastian M. Dawid, Md Habib E. Islam, and Raúl A. Briceño, “Analytic continuation of the relativistic three-particle scattering amplitudes,” *Phys. Rev. D* **108**, 034016 (2023), [arXiv:2303.04394 \[nucl-th\]](#).

[90] Michael Döring, Johann Haidenbauer, Maxim Mai, and Toru Sato, “Dynamical coupled-channel models for hadron dynamics,” *Prog. Part. Nucl. Phys.* **146**, 104213 (2026), [arXiv:2505.02745 \[nucl-th\]](#).

[91] Tyler D. Blanton, Fernando Romero-López, and Stephen R. Sharpe, “ $I = 3$  Three-Pion Scattering Amplitude from Lattice QCD,” *Phys. Rev. Lett.* **124**, 032001 (2020), [arXiv:1909.02973 \[hep-lat\]](#).

[92] Sebastian M. Dawid, Zachary T. Draper, Andrew D. Hanlon, Ben Hörz, Colin Morningstar, Fernando Romero-López, Stephen R. Sharpe, and Sarah Skinner, “Two- and three-meson scattering amplitudes with physical quark masses from lattice QCD,” *Phys. Rev. D* **112**, 014505 (2025), [arXiv:2502.17976 \[hep-lat\]](#).

[93] Raúl A. Briceño, Maxwell T. Hansen, Andrew W. Jackura, Robert G. Edwards, and Christopher E. Thomas, “Isotensor  $\pi\pi\pi$  scattering with a  $\rho$  resonant subsystem from QCD,” (2025), [arXiv:2510.24894 \[hep-lat\]](#).

[94] Yuchuan Feng, Fernando Gil, Michael Döring, Raquel Molina, Maxim Mai, Vanamali Shastry, and Adam Szczepaniak, “A unitary coupled-channel three-body amplitude with pions and kaons,” *Phys. Rev. D* **110**, 094002 (2024), [arXiv:2407.08721](#)

[nucl-th].

[95] Michael Döring, Kanchan P. Khemchandani, and Alberto Martínez Torres, “Revisiting the three-kaon interaction and its relation with  $K(1460)$ ,” (2025), [arXiv:2511.02543 \[nucl-th\]](https://arxiv.org/abs/2511.02543).

[96] Ulf G. Meißner, “Recent developments in chiral perturbation theory,” *Rept. Prog. Phys.* **56**, 903–996 (1993), [arXiv:hep-ph/9302247](https://arxiv.org/abs/hep-ph/9302247).

[97] Barry R. Holstein, “Chiral perturbation theory: An effective field theory,” *Prog. Part. Nucl. Phys.* **61**, 3–18 (2008).

[98] Evgeny Epelbaum, “Nuclear Forces from Chiral Effective Field Theory: A Primer,” (2010) [arXiv:1001.3229 \[nucl-th\]](https://arxiv.org/abs/1001.3229).

[99] Nils Hermansson-Truedsson, “Chiral Perturbation Theory at NNNLO,” *Symmetry* **12**, 1262 (2020), [arXiv:2006.01430 \[hep-ph\]](https://arxiv.org/abs/2006.01430).

[100] Michael C. Birse, “Effective chiral Lagrangians for spin 1 mesons,” *Z. Phys. A* **355**, 231–246 (1996), [arXiv:hep-ph/9603251](https://arxiv.org/abs/hep-ph/9603251).

[101] M. F. M. Lutz and E. E. Kolomeitsev, “On meson resonances and chiral symmetry,” *Nucl. Phys. A* **730**, 392–416 (2004), [arXiv:nucl-th/0307039](https://arxiv.org/abs/nucl-th/0307039).

[102] L. Roca, E. Oset, and J. Singh, “Low lying axial-vector mesons as dynamically generated resonances,” *Phys. Rev. D* **72**, 014002 (2005), [arXiv:hep-ph/0503273](https://arxiv.org/abs/hep-ph/0503273).

[103] Antoni Woss, Christopher E. Thomas, Jozef J. Dudek, Robert G. Edwards, and David J. Wilson, “Dynamically-coupled partial-waves in  $\rho\pi$  isospin-2 scattering from lattice QCD,” *JHEP* **07**, 043 (2018), [arXiv:1802.05580 \[hep-lat\]](https://arxiv.org/abs/1802.05580).

[104] M. Mai, B. Hu, M. Döring, A. Pilloni, and A. Szczepaniak, “Three-body Unitarity with Isobars Revisited,” *Eur. Phys. J. A* **53**, 177 (2017), [arXiv:1706.06118 \[nucl-th\]](https://arxiv.org/abs/1706.06118).

[105] Suh Urk Chung, “SPIN FORMALISMS,” *xxx* (1971), 10.5170/CERN-1971-008.

[106] D. Sadasivan, M. Mai, H. Akdag, and M. Döring, “Dalitz plots and lineshape of  $a_1(1260)$  from a relativistic three-body unitary approach,” *Phys. Rev. D* **101**, 094018 (2020), [Erratum: *Phys. Rev. D* 103, 019901 (2021)], [arXiv:2002.12431 \[nucl-th\]](https://arxiv.org/abs/2002.12431).

[107] A. Dobado and J. R. Peláez, “The Inverse amplitude method in chiral perturbation theory,” *Phys. Rev. D* **56**, 3057–3073 (1997), [arXiv:hep-ph/9604416](https://arxiv.org/abs/hep-ph/9604416).

[108] C. Hanhart, J. R. Peláez, and G. Rios, “Quark mass dependence of the rho and sigma from dispersion relations and Chiral Perturbation Theory,” *Phys. Rev. Lett.* **100**, 152001 (2008), [arXiv:0801.2871 \[hep-ph\]](https://arxiv.org/abs/0801.2871).

[109] Maxim Mai, Chris Culver, Andrei Alexandru, Michael Döring, and Frank X. Lee, “Cross-channel study of pion scattering from lattice QCD,” *Phys. Rev. D* **100**, 114514 (2019), [arXiv:1908.01847 \[hep-lat\]](https://arxiv.org/abs/1908.01847).

[110] A. Gómez Nicola and J. R. Peláez, “Meson meson scattering within one loop chiral perturbation theory and its unitarization,” *Phys. Rev. D* **65**, 054009 (2002), [arXiv:hep-ph/0109056](https://arxiv.org/abs/hep-ph/0109056).

[111] M. Döring, J. Haidenbauer, Ulf-G. Meißner, and A. Rusetsky, “Dynamical coupled-channel approaches on a momentum lattice,” *Eur. Phys. J. A* **47**, 163 (2011), [arXiv:1108.0676 \[hep-lat\]](https://arxiv.org/abs/1108.0676).

[112] Huey-Wen Lin, “Review of Baryon Spectroscopy in Lattice QCD,” *Chin. J. Phys.* **49**, 827 (2011), [arXiv:1106.1608 \[hep-lat\]](https://arxiv.org/abs/1106.1608).

[113] Daniel Mohler, “Review of lattice studies of resonances,” *PoS LATTICE2012*, 003 (2012), [arXiv:1211.6163 \[hep-lat\]](https://arxiv.org/abs/1211.6163).

[114] Martin Lüscher and Ulli Wolff, “How to Calculate the Elastic Scattering Matrix in Two-dimensional Quantum Field Theories by Numerical Simulation,” *Nucl. Phys. B* **339**, 222–252 (1990).

[115] Christopher Michael and I. Teasdale, “Extracting Glueball Masses From Lattice QCD,” *Nucl. Phys. B* **215**, 433–446 (1983).

[116] Benoit Blossier, Michele Della Morte, Georg von Hippel, Tereza Mendes, and Rainer Sommer, “On the generalized eigenvalue method for energies and matrix elements in lattice field theory,” *JHEP* **04**, 094 (2009), [arXiv:0902.1265 \[hep-lat\]](https://arxiv.org/abs/0902.1265).

[117] Michael Peardon, John Bulava, Justin Foley, Colin Morningstar, Jozef Dudek, Robert G. Edwards, Balint Joo, Huey-Wen Lin, David G. Richards, and Keisuke Jimmy Juge (Hadron Spectrum), “A Novel quark-field creation operator construction for hadronic physics in lattice QCD,” *Phys. Rev. D* **80**, 054506 (2009), [arXiv:0905.2160 \[hep-lat\]](https://arxiv.org/abs/0905.2160).

[118] A. Alexandru, C. Pelissier, B. Gamari, and F. Lee, “Multi-mass solvers for lattice QCD on GPUs,” *J. Comput. Phys.* **231**, 1866–1878 (2012), [arXiv:1103.5103 \[hep-lat\]](https://arxiv.org/abs/1103.5103).

[119] William I. Jay and Ethan T. Neil, “Bayesian model averaging for analysis of lattice field theory results,” *Physical Review D* **103** (2021), 10.1103/physrevd.103.114502.

[120] Ethan T. Neil and Jacob W. Sitisson, “Improved information criteria for Bayesian model averaging in lattice field theory,” (2022), [arXiv:2208.14983 \[stat.ME\]](https://arxiv.org/abs/2208.14983).

[121] R. García-Martin, R. Kaminski, J. R. Peláez, and J. Ruiz de Elvira, “Precise determination of the  $f_0(600)$  and  $f_0(980)$  pole parameters from a dispersive data analysis,” *Phys. Rev. Lett.* **107**, 072001 (2011), [arXiv:1107.1635 \[hep-ph\]](https://arxiv.org/abs/1107.1635).

- [122] Dehua Guo, Andrei Alexandru, Raquel Molina, and Michael Döring, “Rho resonance parameters from lattice QCD,” *Phys. Rev. D* **94**, 034501 (2016), [arXiv:1605.03993 \[hep-lat\]](https://arxiv.org/abs/1605.03993).
- [123] Hai-Long Fu, Yong-Hui Lin, Feng-Kun Guo, Hans-Werner Hammer, Ulf-G. Meißner, Akaki Rusetsky, and Xu Zhang, “Exploring Efimov states in  $D^*D^*D^*$  and  $DD^*D^*$  three-body systems,” *JHEP* **07**, 081 (2025), [arXiv:2503.19709 \[hep-ph\]](https://arxiv.org/abs/2503.19709).
- [124] Paulo F. Bedaque, H. W. Hammer, and U. van Kolck, “Renormalization of the three-body system with short range interactions,” *Phys. Rev. Lett.* **82**, 463–467 (1999), [arXiv:nucl-th/9809025](https://arxiv.org/abs/nucl-th/9809025).
- [125] Maxim Mai, Michael Döring, Carlos Granados, Helmut Haberzettl, Ulf-G. Meißner, Deborah Rönchen, Igor Strakovsky, and Ron Workman (Jülich-Bonn-Washington), “Jülich-Bonn-Washington model for pion electroproduction multipoles,” *Phys. Rev. C* **103**, 065204 (2021), [arXiv:2104.07312 \[nucl-th\]](https://arxiv.org/abs/2104.07312).
- [126] Ajay S. Sakthivasan, Maxim Mai, Akaki Rusetsky, and Michael Döring, “Effects of final state interactions on Landau singularities,” *JHEP* **10**, 246 (2024), [arXiv:2407.17969 \[hep-ph\]](https://arxiv.org/abs/2407.17969).